Meteoritics & Planetary Science 40, Nr 9/10, 1513–1536 (2005)
Abstract available online at http://meteoritics.org

Geochemical and petrographic characteristics of impactites and Cretaceous target rocks from the Yaxcopoil-1 borehole, Chicxulub impact structure, Mexico: Implications for target composition

Martin G. TUCHSCHERER[1], Wolf Uwe REIMOLD[1*], Christian KOEBERL[2], and Roger L. GIBSON[1]

[1]Impact Cratering Research Group, School of Geosciences, University of the Witwatersrand,
Private Bag 3, P.O. Wits, 2050 Johannesburg, South Africa
[2]Department of Geological Sciences, University of Vienna, Althanstrasse 14, A-1090 Vienna, Austria
[*]Corresponding author. E-mail: reimoldw@geosciences.wits.ac.za; after January 1, 2006: Uwe.Reimold@museum.HU-Berlin.de

(Received 28 October 2004; revision accepted 10 June 2005)

All tables for this article are available online at http://meteoritics.org.

Abstract–We present major and trace element data as well as petrographic observations for impactites (suevitic groundmass, bulk suevite, and melt rock particles) and target lithologies, including Cretaceous anhydrite, dolomite, argillaceous limestone, and oil shale, from the Yaxcopoil-1 borehole, Chixculub impact structure. The suevitic groundmass and bulk suevite have similar compositions, largely representing mixtures of carbonate and silicate components. The latter are dominated by melt rock particles. Trace element data indicate that dolomitic rocks represented a significant target component that became incorporated into the suevites; in contrast, major elements indicate a strong calcitic component in the impactites. The siliceous end-member requires a mafic component in order to explain the low SiO_2 content. Multicomponent mixing of various target rocks, the high alteration state, and dilution by carbonate complicate the determination of primary melt particle compositions. However, two overlapping compositional groups can be discerned—a high-Ba, low-Ta group and a high-Fe, high-Zn, and high-Hf group. Cretaceous dolomitic rocks, argillaceous limestone, and shale are typically enriched in U, As, Br, and Sb, whereas anhydrite contains high Sr contents. The oil shale samples have abundances that are similar to the North American Shale Composite (NASC), but with a comparatively high U content. Clastic sedimentary rocks are characterized by relatively high Th, Hf, Zr, As, and Sb abundances. Petrographic observations indicate that the Cretaceous rocks in the Yaxcopoil-1 drill core likely register a multistage deformation history that spans the period from pre- to post-impact. Contrary to previous studies that claimed evidence for the presence of impact melt breccia injection veins, we have found no evidence in our samples from a depth of 1347–1348 m for the presence of melt breccia. We favor that clastic veinlets occur in a sheared and altered zone that underwent intense diagenetic overprint prior to the impact event.

INTRODUCTION

Chicxulub (Yucatán Peninsula, Mexico) is the Earth's third-largest known impact structure (Grieve and Therriault 2000). Its formation is widely accepted to have been responsible for the dramatic environmental changes at the Cretaceous/Tertiary (K/T) boundary (e.g., Hildebrand et al. 1991; Swisher et al. 1992; Blum et al. 1993; Ryder et al. 1996; papers in Koeberl and McLeod 2002). Because of its great scientific importance for the understanding of impact cratering processes in general and those related to the K/T mass extinction in particular, the structure was recently drilled by the International Continental Scientific Drilling Program (ICDP) (Dressler et al. 2003). The resulting Yaxcopoil-1 (Yax-1) (Fig. 1) drill core contains a continuous section of impact breccias ~100 m long. Impactite samples are of particular interest, as they can provide constraints on the pressures and temperatures experienced by target rocks and can give clues to the mode of impactite formation and deposition during impact cratering. Chemical analysis of impactites also constrains mixing between the various target rocks and the bolide, and provides information on post-impact alteration processes.

The major and trace element compositions of target rocks

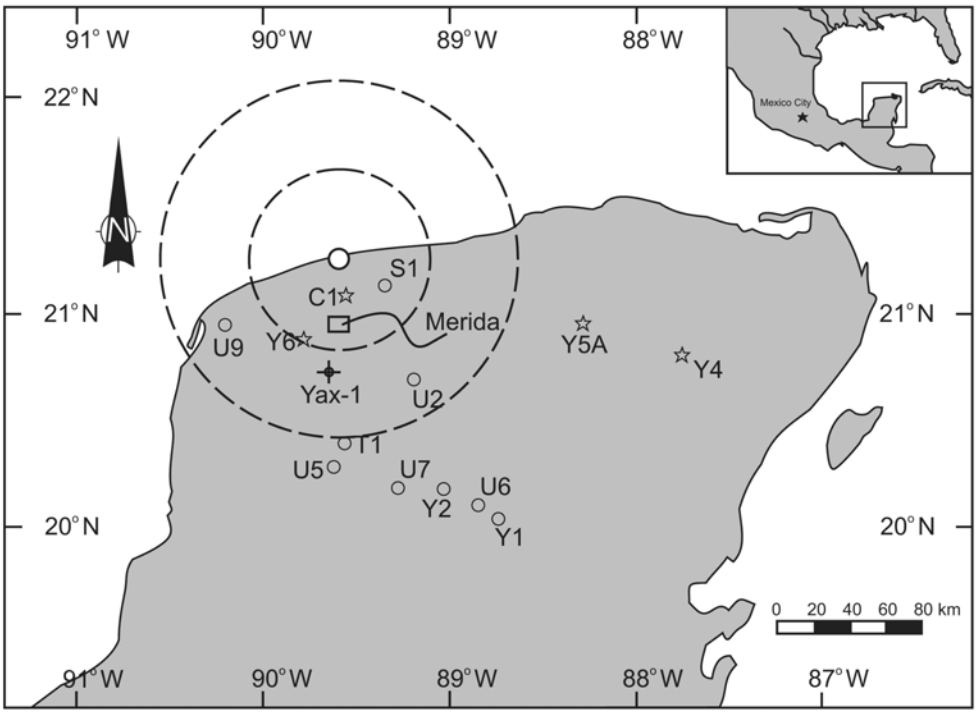

Fig. 1. Location of the Yaxcopoil-1 (Yax-1) and other boreholes within and around the Chicxulub impact structure on the northeastern segment of the Yucatán Peninsula of Mexico. Boreholes mentioned in the text are shown as stars. The innermost dashed circle represents the inferred extent of the initial transient cavity as postulated by Morgan et al. (2002). The outer dashed circle represents the estimated crater edge (rim) as determined by seismic surveying of the outermost inward-facing scarp (Morgan et al. 2002).

and their contribution to the various units of the Chicxulub impactites, as well as of the suevitic groundmass, bulk suevite, and melt rock particle fractions, are the prime focus of this paper. This work was done in order to constrain the dominant geochemical components that are part of the impactite composition and to investigate their distribution and mixing throughout the interval. As part of our investigation of the Cretaceous section below the impactite interval, breccia veinlets in the 1347–1348 m depth interval were investigated with regard to their possible origin as impact melt.

THE YAXCOPOIL-1 BOREHOLE

Drilling into the Yucatán subsurface extended to a depth of 1511 m and intersected approximately 795 m of post-impact Tertiary carbonate rocks, 100 m of impactites, and 615 m of pre-impact Cretaceous rocks (Fig. 2). The impactites are composed of suevitic and impact melt breccias, both of which have undergone significant alteration (Dressler 2004; Ames et al. 2004; Kring et al. 2004; Hecht et al. 2004; Kenkmann et al. 2004; Schmitt et al. 2004; Stinnesbeck et al. 2004; Stöffler et al. 2004; Wittman et al. 2004; Zurcher et al. 2004). While most research groups have adopted the original six-fold impactite stratigraphy of Dressler et al. (2003) (cf. Fig. 2), we subdivide the Yax-1 impact breccias into five units based on macro- and microscopic observations (according to Tuchscherer et al. 2004a).

The uppermost unit 1, between 795 and 823 m, is defined as a reworked suevite deposit that contains foraminifera and lithic carbonate clasts with numerous self-supported melt rock particles. The melt particles are subrounded to subangular, green when palagonized, and contain distinct perlitic devitrification textures. A subtle coarsening of the lithic clasts and melt rock particles is noticed with depth. Similar to unit 1, all unit 2 (822.86–845.80 m) melt rock particles are altered green; pervasive conversion of glass and clastic components to phyllosilicates is characteristic of these units. Units 1 and 2 contain high abundances of the large ion lithophile (LIL) elements Rb and Cs. This alteration feature is typical of palagonized volcanic glasses (Staudigel and Hart 1983; Jercinovic et al. 1990). In contrast, unit 3 (845.80–861.06 m) has variegated melt particles that are less altered. The groundmass of units 2 and 3 is rich in volatiles, silicon, and alkali elements, and contains disseminated calcite grains (see Tuchscherer et al. 2004a for more details). The calcite grains have comparatively larger grain sizes toward unit 3, possibly indicating a thermal effect from the underlying mass of green impact melt rock (unit 4, 861.06–884.92 m). Similar metamorphism has also been observed in the so-called “lower suevite” of the Y-6 borehole (Claeys et al. 2003). Unit 4 represents a uniformly green, brecciated, massive impact melt

rock. It does not have the LIL element signature that characterizes the upper altered units, indicating its overall green color may represent its primary composition (see, e.g., Tuchscherer et al. 2004b). Geochemical investigations indicated this melt rock has a composition that is slightly more mafic than brown melt particles found in units 1 to 3, i.e., it contains more FeO_{tot}, MgO, but less CaO (Tuchscherer et al. 2004b). The impact melt rock has abundant microlites, small lithic and monomineralic clasts derived from the crystalline basement, and abundant fractures and veins filled with phyllosilicate. It also displays fluidal textures (schlieren). The lowermost unit, a variegated polymict impact melt breccia or suevite (unit 5, 884.92–894.94 m), comprises discrete siliceous melt particles that are fluidal to angular in shape. They are suspended in a fine-grained calcitic and dolomitic groundmass that could represent either authigenic carbonate or a crystallized impact melt (e.g., Dressler et al. 2004; Tuchscherer et al. 2004a).

The Tertiary rocks overlying the impactite sequence are composed of interlayered carbonaceous siltstones, calcarenite, and rare conglomerate and turbidite (Dressler 2002, personal communication). The underlying (895–1511 m), presumably Cretaceous (Kenkmann et al. 2004; Stinnesbeck et al. 2004; Wittmann et al. 2004) rocks consist of anhydrite, dolomite, and argillaceous limestone, with small intervals of conglomerate (Fig. 2). Several breccia horizons have been observed at 909–910, 916, 1035–1036, and 1347–1348 m; lithic breccias at 1314–1316, 1341, 1398–1399 m; and black oil-bearing shale layers at 1350, 1369, 1372, 1382, 1394, 1397, 1399, and 1420 m depths. Several thick, brittle deformation zones between 1310 and 1400 m and from 1496 to 1511 m have also been identified (for further background on the Cretaceous interval, see Kenkmann et al. 2004; Stinnesbeck et al. 2004; and Wittmann et al. 2004).

SAMPLES

Thirty-six samples from the impactite interval and 27 samples from the Cretaceous interval (Fig. 2) were analyzed. This includes 8 suevitic groundmass samples (from 825.43, 825.43, 827.13, 835.14, 836.98, 836.98, 888.92, and 892.55 m depths), 15 bulk suevite samples (from 2 × 805.34, 809.7, 810.84, 815.8, 816.62, 827.13, and 846.01, 2 × 846.80, 2 × 851.15, 860.4, 888.09, and 894.14 m depths), 10 individual melt rock particles (from 809.7, 810.84, 825.43, 835.14, 840.3, 840.30, 851.15, 878.09, 882.45, and 892.55 m depths), and 3 lithic clasts (from 824.03, 888.09, and 888.92 m depths) from the impact breccia. The Cretaceous samples comprise 1 anhydrite (1314.83 m), 15 dolomite (1314.83, 2 × 1315.86, 2 × 1316.06, 1341.61, 1341.82, 1342.91, and 1347.56, 2 × 1348.31, 1369.52, 1372.87, 1381.64, and 1397.82 m), 5 argillaceous limestone and argillaceous dolomite (2 × 1381.64, 1397.82, 1398.25, and 1399.07 m), 4 oil shale (1369.52, 1372.87, 1394.02, and 1397.82), and 4 dolomite plus oil shale (1369.52, 1381.64, 1395.19, and 1399.07 m) samples. The dolomite samples in particular originate from sections of massive dolomite between 1372.87 m and 1381.64 m, fractured dolomite from 1314.83, 1315.86, and 1369.52 m, and a monomictic dolomitic breccia from 1316.06 m. A polymict breccia was also sampled from an interval between 1341.82 and 1342.91 m, as well as a brecciated blue-green alteration zone with anhydrite veining from the interval between 1347 and 1348 m.

Hand sample descriptions and some microscopic observations are summarized in Table 1 (all tables are available online at http://meteoritics.org), and selected images of off-cuts are shown in Fig. 3. The groundmass from unit 1 could not be separated due to its clast-supported character (Fig. 3a). The analyzed bulk suevite samples have abundant but variable amounts of melt rock particles (Table 1). This group of samples is green to variegated in color, depending on which unit the samples originated from. Examples are shown in Figs. 3a, 3d, 3g, 3h, and 3j. Duplicate analyses were obtained for samples from 805.34, 846.80, and 851.15 m depths. Samples that have few melt particles are generally gray, and are dominated by the carbonate-rich groundmass (Figs. 3c, 3e, and 3j).

Three individual clast samples, a finely laminated gneiss (Fig. 3b), a dolomitic limestone (Fig. 3h), and a granodioritic clast (Fig. 3i) (lithologies classified according to hand sample observation), were separated from the suevitic groundmass. For petrographic characteristics of these inclusions, see Table 1 and Tuchscherer et al. (2004a). Cretaceous rocks illustrated in Fig. 3 include anhydrite (Fig. 3k), a highly brecciated dolomite (Fig. 3l), a thin oil-shale vein (Fig. 3m), and an argillaceous dolomite sample showing stylolitic dissolution texture (Fig. 3n).

ANALYTICAL METHODS

Trace element as well as Na, K, and Fe abundances were obtained by Instrumental Neutron Activation Analysis (INAA) (for methodology, precision, and accuracy details, see Koeberl 1993). Ten Cretaceous samples (one anhydrite, six dolomite, one oil shale, and two argillaceous limestone samples) (Table 6) were analyzed for their major element compositions by standard X-ray fluorescence spectrometry (XRF) at Setpoint Laboratories in Johannesburg, South Africa, whereas the remaining samples were too small to allow full major element analysis. For major element precision and accuracy values see Tuchscherer et al. (2004b). Sulfur contents were determined by direct combustion analysis using a LECO sulfur determinator SC132 instrument at the University of the Witwatersrand (for details concerning methodology, precision, and accuracy, see Tuchscherer et al. 2004b). Scanning electron microscopy (SEM) was done at the Council for Geoscience in Pretoria, South Africa with a Leica 440 Stereoscan instrument equipped with a LINK OXFORD

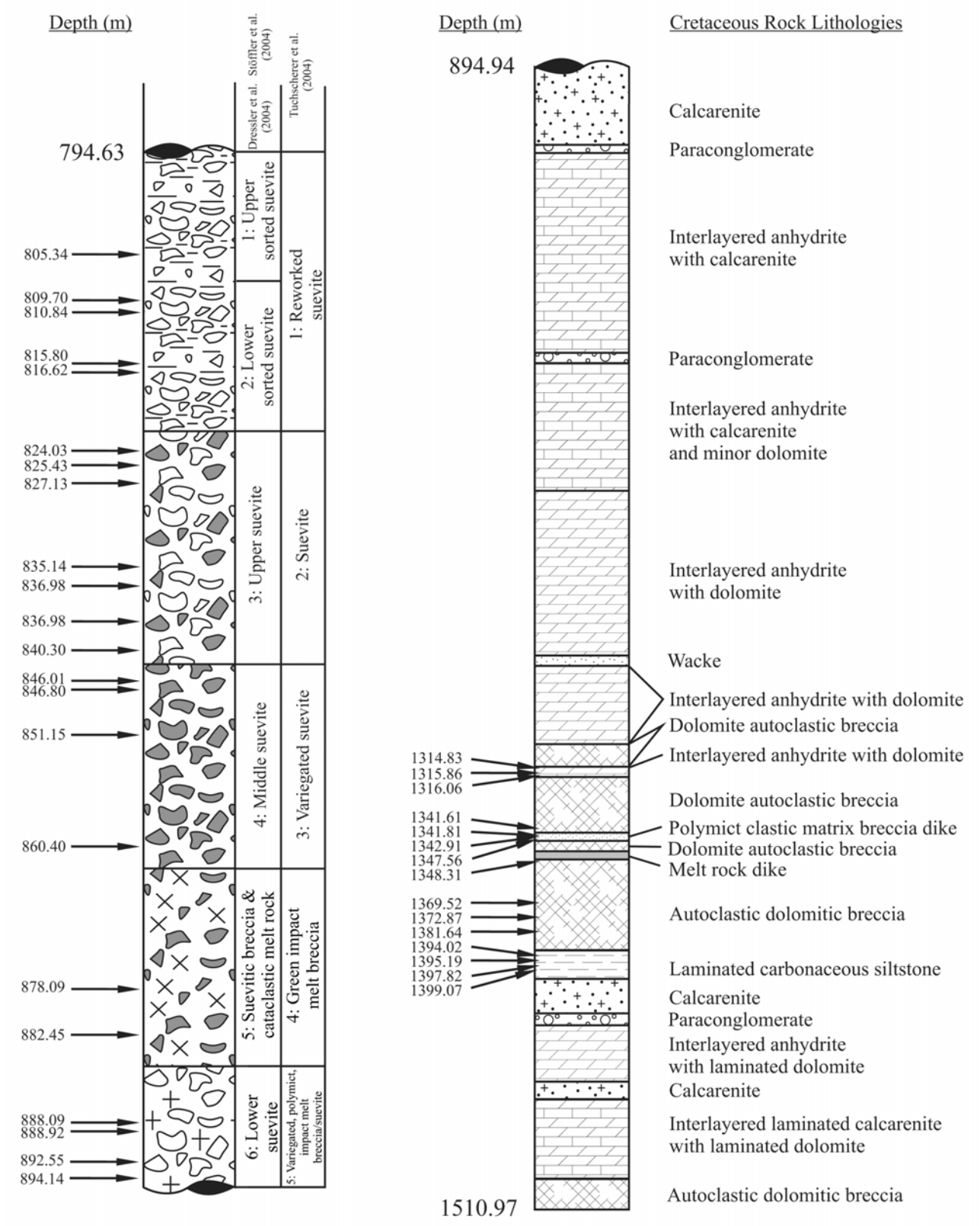

Fig. 2. Core-log and stratigraphy of the Yaxcopoil-1 borehole, with the depths of the samples used in this study. The stratigraphic subdivisions after Dressler et al. (2004), Stöffler et al. (2004), and Tuchscherer et al. (2004) are also shown and juxtaposed to the log.

EDS X-ray analysis system operating at 20 kV and 2 nA working conditions at 25 mm working distance. Two bulk sample powders from 1347.56 and 1348.31 m were also analyzed for their mineralogical content by X-ray diffraction (XRD) with the University of the Witwatersrand's Phillips PW 1710 instrument.

CALCULATION OF END-MEMBER AND CRETACEOUS TARGET ROCK INTERVAL COMPOSITIONS

End-member compositions for the suevite section of the Yax-1 borehole were calculated by linear regression analysis of the major and trace element compositions of the impactites from the data of Tuchscherer et al. (2004b). This was done using the "LINEST" function in Microsoft Excel. The carbonate end-member of the Yax-1 impactites (denominated "CEMY") was derived by plotting all elements versus SiO_2, extrapolating a best-fit linear regression line for each element, and calculating the respective element abundance for a silica content of 4 wt%. This silica value was used, as it represents our best estimate of the average silica abundance of the Cretaceous target rock interval of the Yax-1 borehole (denominated "CTIY") and thus provides a good means for comparing all major and trace element abundances of carbonate-dominated and silicate components. The siliceous end-member of the Yax-1 impactites ("SEMY") was calculated by plotting all elements versus CaO and extrapolating the best-fit linear regression line for each element, also based on the results of Tuchscherer et al. (2004b). The respective element abundances were then calculated for a CaO content of 5.2 wt%. This CaO value was used, as it is identical to the average CaO composition of unit 4 and the CaO content in previously analyzed impact melt rock samples from other Chicxulub boreholes, e.g., from the C1 borehole (Sharpton et al. 1992; Kring 1997). Although higher CaO values have been reported for impact melt rocks from the Y6 and Yax-1 boreholes (Schuraytz et al. 1994; Claeys et al. 2003; Ames et al. 2004; Schmitt et al. 2004), we used the lowest-published CaO abundances of bulk rock samples in order to provide a good SEMY composition. This is also done in order to reduce the diluting effects that any minor carbonate presence may cause. The calculated end-member compositions are listed in Table 2. Correlation coefficients (R^2), slopes (m), y-intercepts (b), respective least-square standard errors, and y-estimate least-square standard errors for the elements plotted against SiO_2 and CaO are presented in Table 2.

An average composition for CTIY (Table 2) was estimated based on a detailed core log provided by B. O. Dressler (personal communication, 2002) with the following lithological proportions: dolomite (63 vol%), anhydrite (27 vol%), and argillaceous limestone (10 vol%). The averaged dolomite composition from this work, two anhydrite analyses from Schmitt et al. (2004), and the average argillaceous limestone of this study were used.

RESULTS

Petrography of Cretaceous Rocks

Petrographic observations were made on selected samples in order to understand the mineralogy and, thus, the compositions of the rocks. Details on our Cretaceous samples are presented in Table 3. In brief, anhydrite is greyish white in hand sample (Figs. 3k and 4) and has moderate birefringence under cross-polarized light. Crystals are usually tabular and elongated, and some occur in seemingly fluidal arrangements. Grains can be up to 1 mm wide along the crystal short axis. Dolomite is beige/brown in hand samples and shows very high birefringence. Crystals are typically fine-grained and <0.05 mm, but are locally euhedral and of larger size (~0.2 mm), where they are found in association with phyllosilicates. Argillaceous dolomite samples are typically grayish black and locally finely laminated. In such cases, dolomite crystals are very fine-grained and occur in dark gray phyllosilicate.

The Yax-1 borehole is located in a major deformation zone that comprises a series of slumped blocks between 40 and 65 km from the crater center, as determined by seismic profiling (e.g., Morgan et al. 1997). Selected photographs of core samples from the intersected Cretaceous rocks show some characteristic deformation features. Figs. 4a and 4b show several anhydrite samples from various depths that have fluidal textures that may be typical of solution collapse. The dolomitic host rocks and the anhydrite are not fractured (Fig. 4b). This may indicate that the rock is younger than the intense brecciation observed in dolomitic rocks. The anhydrite sample shown in Fig. 4a (see also Table 3) displays crystals (<0.05 mm) that seem to be part of a fluidal pattern. Anhydrite is intercalated with a brownish mixture of dolomite and phyllosilicates, with some fine-grained, disseminated pyrite. The sample from 1394.02 m also shows this fluidal-textured anhydrite, but also has a black hydrocarbon vein (Fig. 4b). Figure 4c reveals anhydrite and dolomite clasts that are contained in an oil shale. Again, no extensive brittle fracturing, as is seen in the dolomite, can be discerned. Thus, it is reasonable to interpret the occurrence of fluidal anhydrite (Figs. 4a and 4b) and the anhydrite clasts in Fig. 4c as the product of dissolution-related processes, in agreement with the observations of Stinnesbeck et al. (2004). However, we note that monomictic breccias several centimeters thick, with sharp contacts to the footwall that could be indicative of high strain rates unique to a single slip event typical of impacts (e.g., Kenkmann 2002), have been found in at least one massive anhydrite horizon at 1314.83 m. This indicates that not all anhydrite dissolution features postdate the pervasive brittle deformation event.

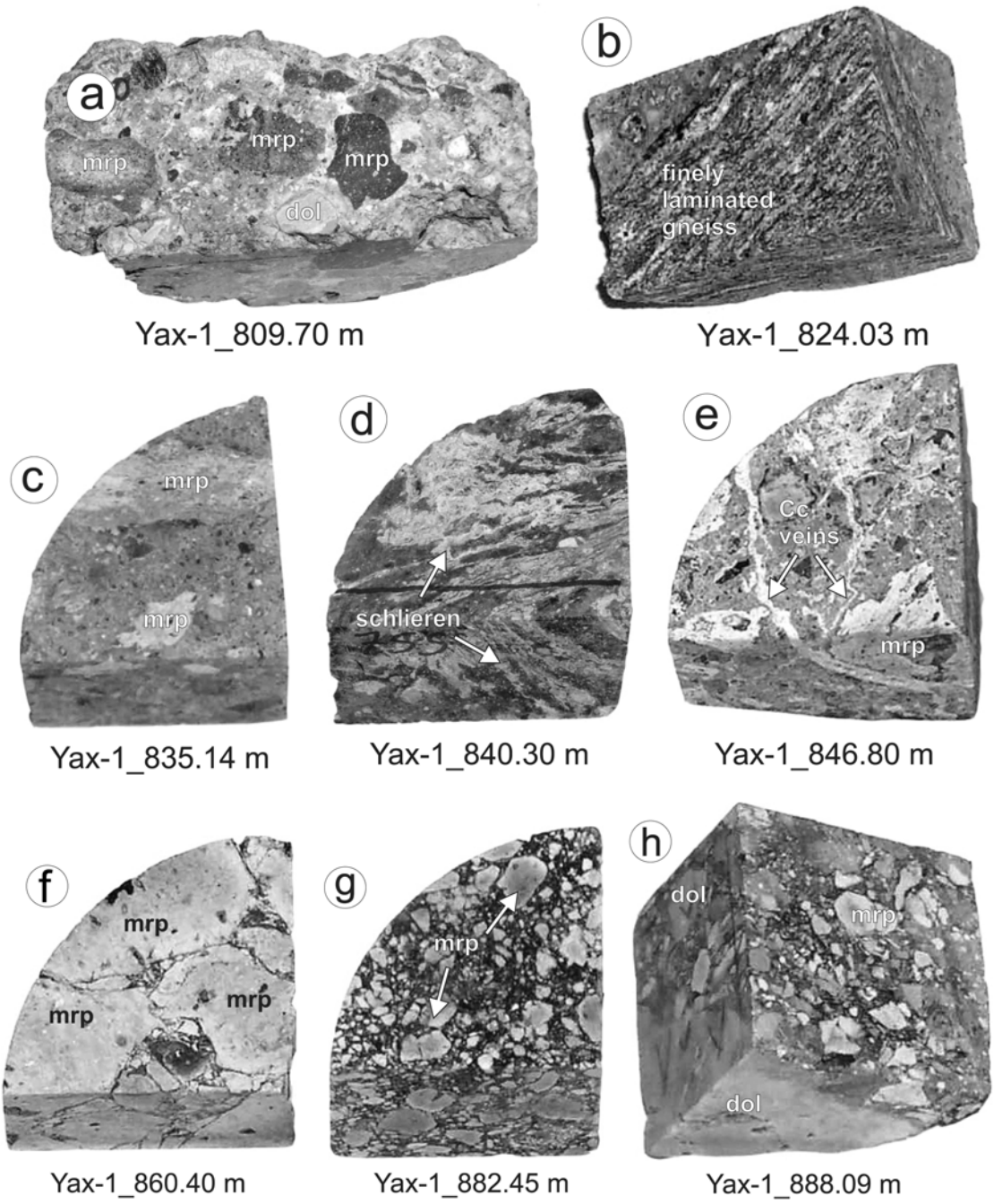

Fig. 3. Images of selected impactite samples used in this study. a) Suevite of unit 1 showing various reworked subrounded melt rock particles and lithic clasts of variable size that are self-supported (sample long axis = 6.35 cm). b) A finely laminated gneiss clast suspended in suevitic groundmass of unit 2 (sample long axis ~3 cm). c) Unreworked suevite containing numerous melt rock particles of various sizes and alteration state that are groundmass-supported. The melt rock particles show schlieren textures and are subrounded and elongated, which is indicative of flow; unit 2, core radius ~3 cm. d) A massive brown melt particle showing schlieren textures, which are indicative of flow and incomplete mixing of felsic and mafic components. Small undigested lithic clasts of <0.5 cm size can be discerned suspended in the melt rock particle; unit 2, core radius ~3 cm. e) Unreworked suevite of unit 3 containing variegated melt rock particles of various sizes that are subangular to subrounded and are groundmass-supported. Numerous calcite veins <0.5 cm wide cut across the groundmass (core radius ~3 cm). f) A massive impact melt rock agglomerate from the bottom of unit 3, similar to the massive impact melt rock of unit 4. The dark veins are rich in phyllosilicate and calcite and represent individual melt particle boundaries (core radius ~3 cm). g) Subrounded to rounded melt particles suspended in a dark grey, fine-grained, calcite-rich groundmass from unit 4 thought to represent an impact melt (core radius ~3 cm). h) Various melt rock particles and lithic clasts that are subrounded and supported by a dark grey, calcite-rich groundmass from unit 5 (core radius ~3 cm). Abbreviations: anh = anhydrite, Cc = calcite, dol = dolomite, mrp = melt rock particles, os = oil shale.

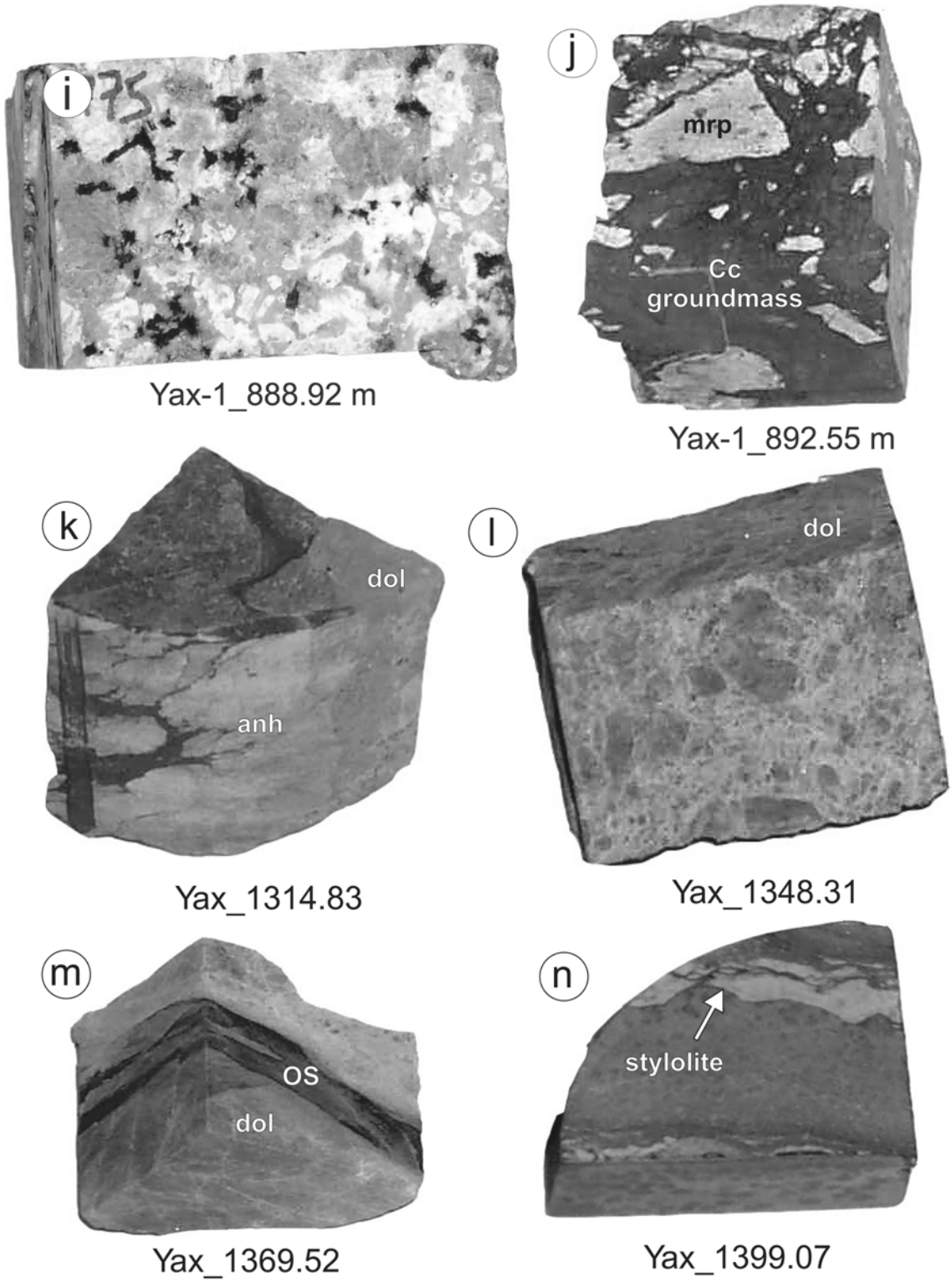

Fig. 3. *Continued*. Images of selected impactite samples used in this study. i) A medium-grained granodiorite clast from unit 5 (sample long axis ~3 cm). j) Groundmass-supported angular melt particles of unit 5. The groundmass comprises fine-grained calcite that may be an impact melt (sample width ~2.5 cm). k) Anhydrite intergrown with phyllosilicates in dolomite (core radius ~3 cm). l) Highly fractured and brecciated dolomite (sample long axis ~4 cm). m) Thin oil shale horizon in dolomite (sample width ~4 cm). n) Argillaceous limestone with dissolution features (stylolite; sample long core axis ~3 cm). Abbreviations: anh = anhydrite, Cc = calcite, dol = dolomite, mrp = melt rock particles, os = oil shale.

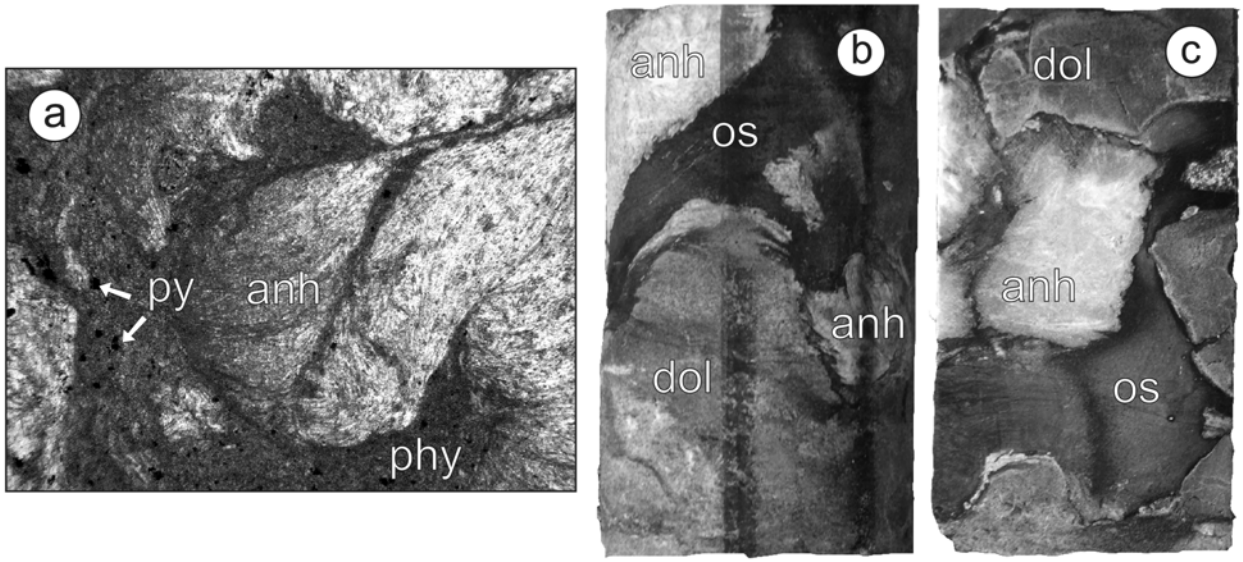

Fig. 4. Anhydrite in the Yax-1 borehole. a) Fluidal-textured anhydrite (anh) intercalated with phyllosilicates (phy). Note the disseminated pyrite (py) in the phyllosilicates. Sample depth = 1314.80 m, width of field of view ~4 mm (long axis), plane polarized light. b) Anhydrite interlayered with dark opaque oil shale (os) hosted by dolomite (dol); sample depth = 1394.02 m, core width = 6.35 cm (short axis). c) Blocky anhydrite and dolomite in oil shale groundmass; sample depth = 1394.12 m, core width = 6.35 cm (short axis).

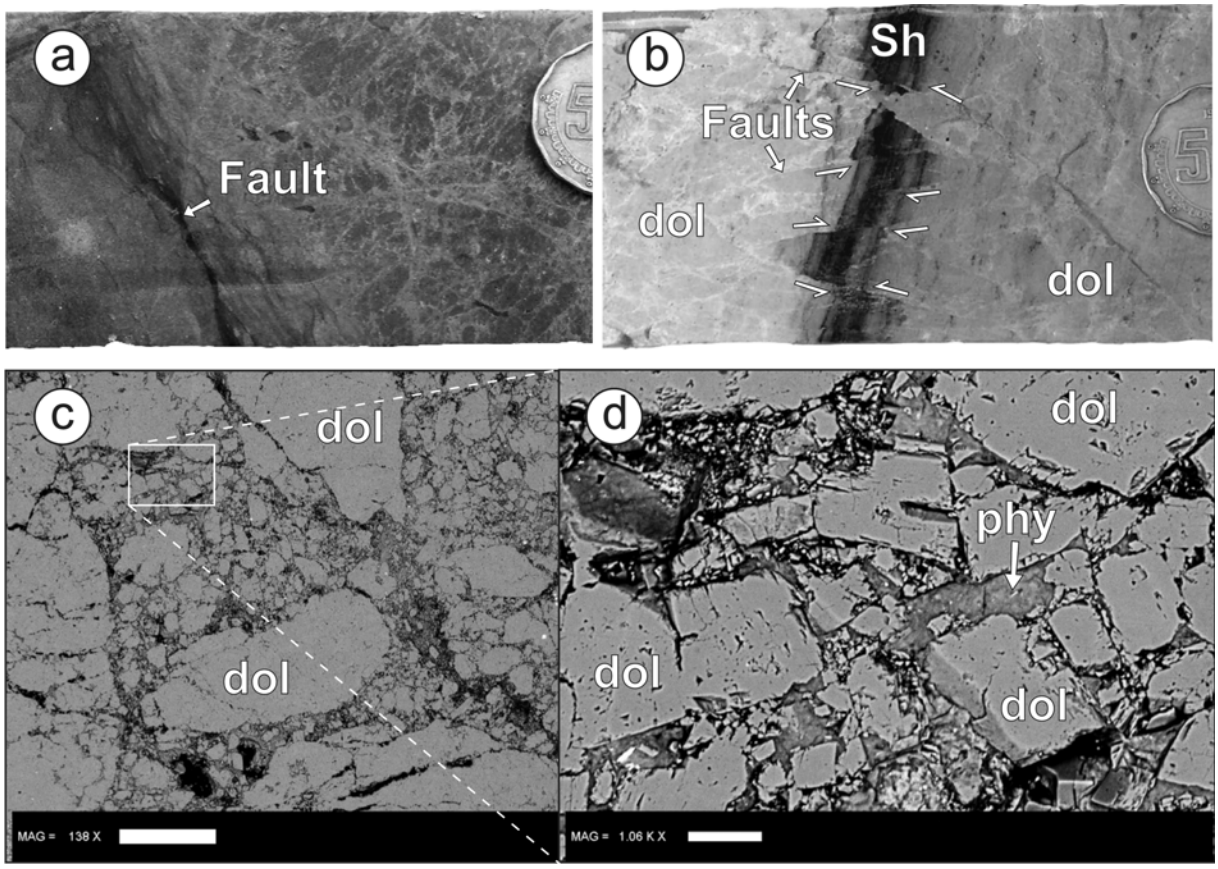

Fig. 5. Brittle deformation in dolomitic rocks. a) Highly fractured dolomitic rocks. Sample depth = 1342.13 m, core width = 6.35 cm (short axis). b) Highly faulted shale (Sh) horizon bounded by shattered dolomite (dol). Sample depth = 1315.86 m, core width = 6.35 cm (short axis). c) Backscattered electron image of brittle brecciated dolomite. Sample depth = 1348.30 m, scale bar = 1 mm. d) Close-up of shattered dolomite in (c). Note the occurrence of phyllosilicates (phy) in interstices. Scale bar = 50 μm.

Massive dolomite intervals are common in the Cretaceous section. On a macroscopic scale, they are typically shattered and locally faulted (e.g., Figs. 5a and 5b). This brittle deformation is observed as finely fractured dolomite crystals occurring along thin (0.2–1 mm) hairline fissures. Under the SEM (Figs. 5c and 5d), fracturing is pervasive to the micrometer scale. No evidence for dissolution and recrystallization of the fine-grained dolomite is observed at this scale in this sample. However, fracturing may have enhanced the porosity of the rock, thereby enabling the infiltration of K-rich fluids, as observed in the form of patches of secondary illite (as determined by XRD). This fracturing can be so pervasive that fine-grained, subrounded dolomitic fragments (Fig. 5c) may be suspended in a groundmass composed of smaller fragments of dolomite (Fig. 5d).

A sample of the massive polymict clastic breccia carries fragments of various compositions and is bounded by a highly fractured dolomitic rock (Figs. 6a and 6b). The breccia itself does not register any post-emplacement deformation. It comprises subangular fragments of anhydrite, dolomite, and argillaceous limestone or shale, and the groundmass consists primarily of similar, yet smaller, lithic fragments (Figs. 6a and 6b).

Figure 7a reveals numerous fractures (outlined in white) and undulating discontinuities (stylolites) that cross-cut a dolomite, anhydrite, and phyllosilicate rich breccia. Associated with this interval is a highly brecciated dolomite that is pervaded by interstitial anhydrite (Fig. 7b). The brecciated alteration zone is characterized by an unusual blue color. Thin repetitive bands, which are blue in the actual hand sample, can be discerned in Fig. 7c. These bands are characterized by alternating concentrations of interstitial illite and dolomite (Fig. 7d). The occurrence of illite was determined by X-ray diffractometry on samples 219 and 226. Euhedral crystals of pyrite and zoned dolomite are suspended in this groundmass (Figs. 7d and 7e). The dolomite crystals pictured are characteristically euhedral and of the same size, i.e., planar and unimodal, or idiotopic (Warren 2000). The characteristic zonation is defined by cloudy centers and clear rims. This texture is apparently typical of primary crystal growth at temperatures below 50 °C (Gregg and Sibley 1984). Our microscopic observations did not reveal any impact-related microfeatures.

Several argillaceous limestone samples were analyzed from below 1381 m depth (Fig. 2). They contain small calcite crystals (~0.025 mm) intercalated with abundant phyllosilicate and opaques. Locally, black, oil-bearing veins truncate fresh samples of this argillaceous limestone. The oil-bearing horizons throughout the Cretaceous interval of the Yax-1 borehole vary in width from ~5 mm to 1 cm; examples are shown in Figs. 8a–c. In hand samples, this material is very fine-grained, and locally it contains small, subangular dolomite fragments that could originate from the immediate

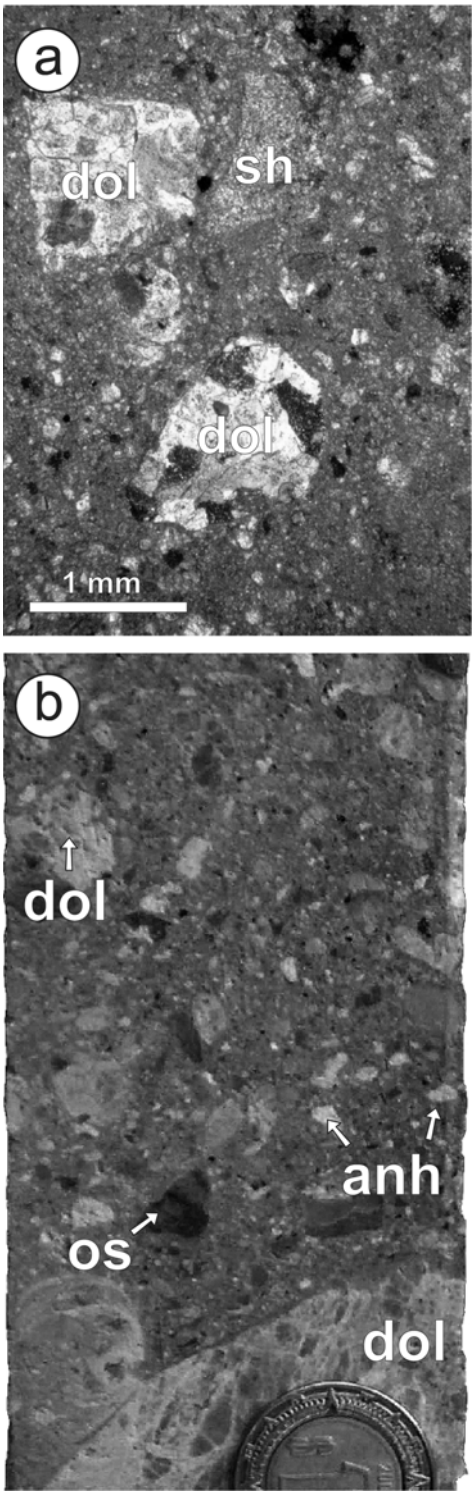

Fig. 6. Polymict lithic breccia from 1342.91 m depth. dol = dolomite, sh = shale, os = oil shale, anh = anhydrite. a) A microscopic image of the polymict lithic breccia dike; crossed polarizers, field of view ~4 mm (long axis); note the breccia nature of the groundmass and the heterogeneous composition of lithic fragments. b) A macrophotograph of the same breccia. Note the heterolithic nature and subangular character of individual fragments. Coin diameter = 2 cm.

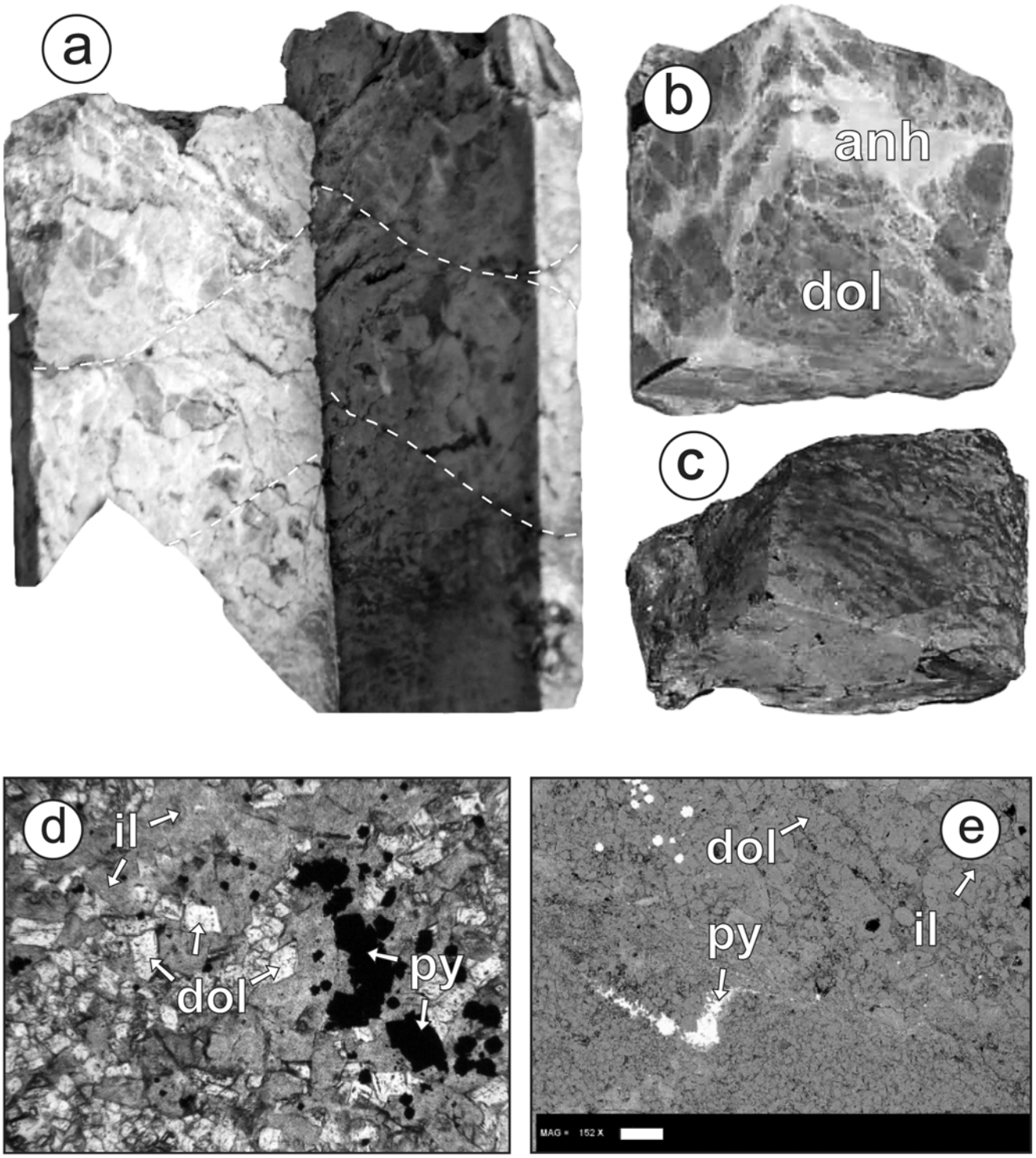

Fig. 7. Samples from the brecciated interval between 1347 and 1348 m. a) A macrophotograph of the halved core from a depth of 1347.5 m showing the heterogeneous and fragmental nature of clasts within the interval. Dashed lines indicate fault zones; core width = 6.35 cm (short axis). b) Anhydrite (anh) veinlets pervading highly brecciated dolomite (dol) interval. Sample depth = 1348.30 m; sample height and width is ~2 cm. c) Core off-cut showing fluidal, dark bands between lighter dolomitic layers. Sample depth = 1347.60 m; sample width ~3 cm (short axis). d) Microscopic image of the undulating, dark banded sample shown in Fig. 7a, with illite (il) relationship with dolomite grains and euhedral pyrite (py) crystals. Sample depth = 1347.60, field of view ~4 mm (long axis), plane-polarized light. e) Backscattered electron image of very fine-grained dolomite with pyrite (same sample as in Fig. 7d). Toward the top right, dolomite crystals are observed interspersed with phyllosilicate minerals. Sample depth = 1347.60 m. Scale bar = 200 μm.

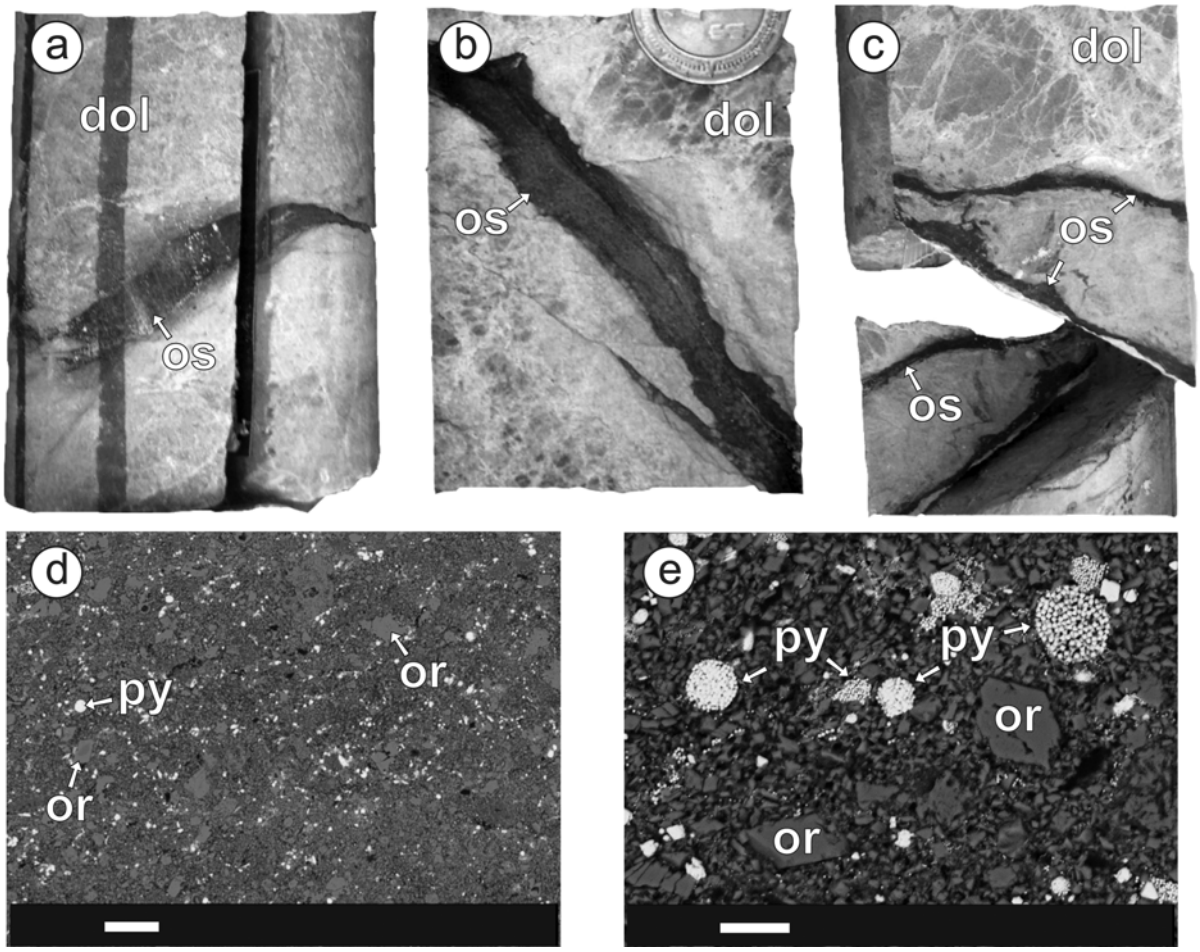

Fig. 8. Black, oil-bearing shale layers within the Cretaceous sequence of the Yaxcopoil-1 borehole. a) Undulating oil-shale (os) vein within dolomite (dol). Sample depth = 1369.52 m, core width = 6.35 cm (short axis). b) A 1-cm-thick oil-bearing shale vein. Note the offshoot at the lower right and the fractured character of the host dolomite. Sample depth = 1373.59 m, core width = 6.35 cm (short axis). c) Anastomosing network of oil-bearing shale layers, ~0.5 cm thick. Sample depth = 1372.87 m, core width = 6.35 cm (short axis). d) A backscattered electron image of a typical oil-bearing shale. Note the disseminated pyrite (py) and orthoclase (or). Sample depth = 1394.00 m, scale bar = 100 μm. e) A backscattered electron image of spherical pyrite aggregates (framboids) and orthoclase within oil-shale. Sample depth = 1394.00 m. Scale bar = 10 μm.

host rock (Fig. 8b). SEM analysis shows that the veins contain disseminated euhedral adularia crystals and spherical pyrite framboids in a phyllosilicate matrix (Figs. 8d and 8e). Such pyrite framboids are typical of kerogen-rich rocks such as oil shales (e.g., Combaz 1970), but also occur in sedimentary rocks formed in reducing environments (e.g., Wilkin et al. 1996; Butler and Rickard 2000). Each pyrite crystal is coated by a thin film of organic material, and the framboids may act as a trace element trap (Tissot and Welte 1978).

Impactite Geochemistry

Major and trace element data of impactites are shown in Table 4; averages for the suevitic groundmass, bulk suevite, and melt rock particles are given in Table 5. For comparison, the impactite carbonate and silicate end-member compositions, calculated according to the procedures outlined in the previous section, are shown in Figs. 9–14.

The major elements Na_2O, K_2O, and FeO_{tot} show considerable compositional variation (Table 4). The melt particles have the highest Na_2O, K_2O, and FeO_{tot} abundances, followed by the groundmass, and the bulk suevite samples (Table 5; Figs. 9a and 9b). However, much overlap exists, especially for the Na_2O and K_2O abundances of the bulk suevite samples and groundmass fractions. The FeO_{tot} content of melt particles is well-constrained, as seen in the 2σ standard deviation (Table 5) when compared to the suevitic groundmass and the bulk suevite (Figs. 9b, 10b, and 12). Among the target rock clasts, the gneiss has the highest iron content (4.7 wt%), followed by the granodiorite (2.11 wt%) and the dolomite (0.08 wt%). The granodiorite has the highest potassium content (4.18 wt%), followed by the gneiss (2.70 wt%) and dolomite (0.23 wt%).

The LIL elements show variable concentrations (Table 5; Fig. 10). Comparing the suevitic groundmass, bulk suevite, and melt particle suites, no specific trends can be established.

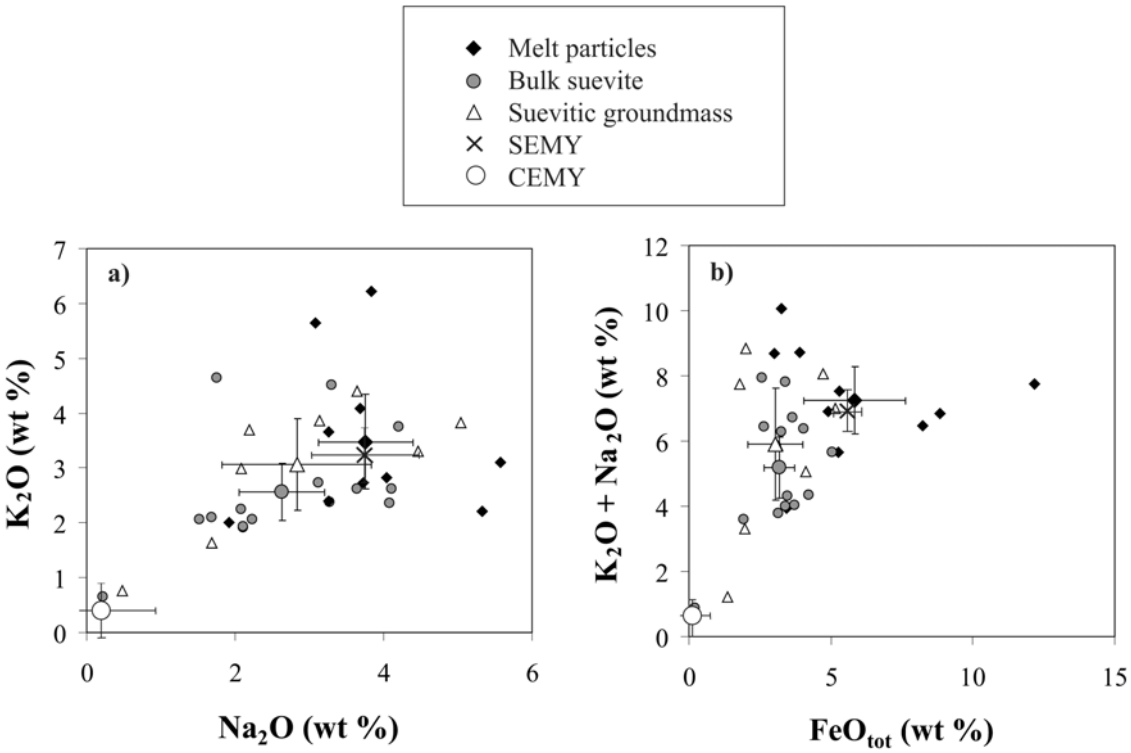

Fig. 9. Binary major element plots showing elemental abundances in all suevitic and melt particle samples analyzed here, as well as for the average compositions for the suevitic groundmass (n = 8), bulk suevite (n = 15), melt particles (n = 10), SEMY (siliceous end-member for the Yax-1 impactites), and CEMY (carbonate end-member for the Yax-1 impactites) of the Yax-1 impactites. Error bars represent 2σ standard deviations plotted for the averaged compositions (melt particles, bulk suevite, and suevitic groundmass), whereas error bars for the end-member compositions represent calculated least-square standard errors for the y-estimate standard error presented in Table 2. a) K_2O versus Na_2O; b) $K_2O + Na_2O$ versus FeO_{tot}. Data in wt%.

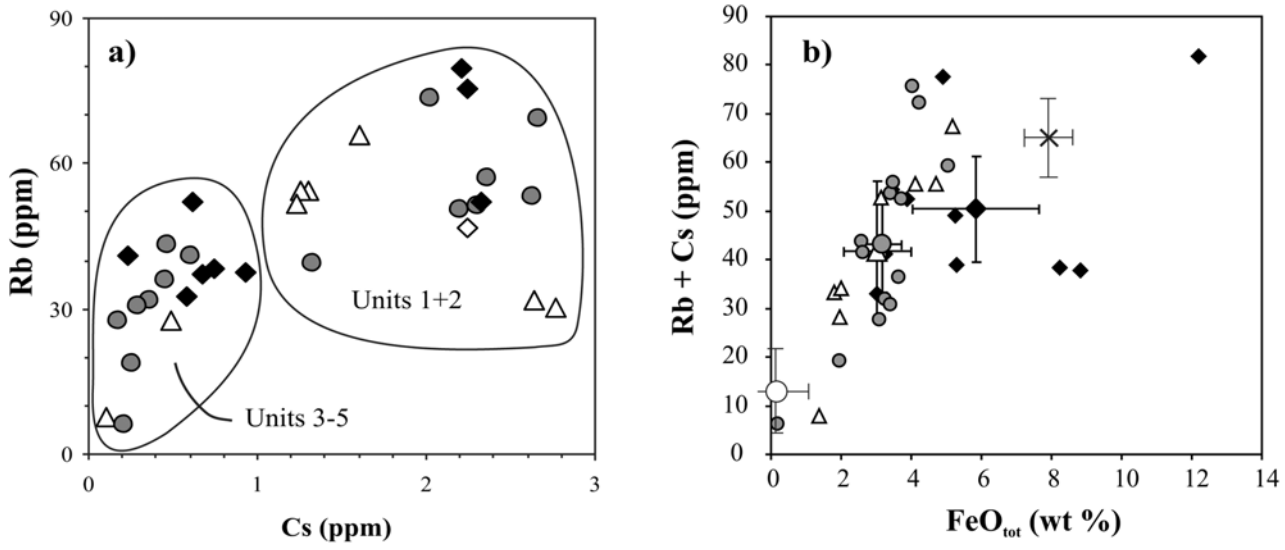

Fig. 10. Binary diagrams for selected large ion lithophile (LIL) elements. a) Rb versus Cs plot for melt particles, suevitic groundmass, and suevitic samples of the Yax-1 impactite interval (see Fig. 9 for legend). b) Rb + Cs versus FeO_{tot} plot showing all samples, averaged compositions for the suevitic groundmass (n = 8), bulk suevite (n = 15), melt particles (n = 10), SEMY (siliceous end-member for the Yax-1 impactites) and CEMY (carbonate end-member for the Yax-1 impactites); error bars represent 2σ standard deviations for averaged compositions and the least square y-estimate standard errors (Table 2) for the end-member compositions.

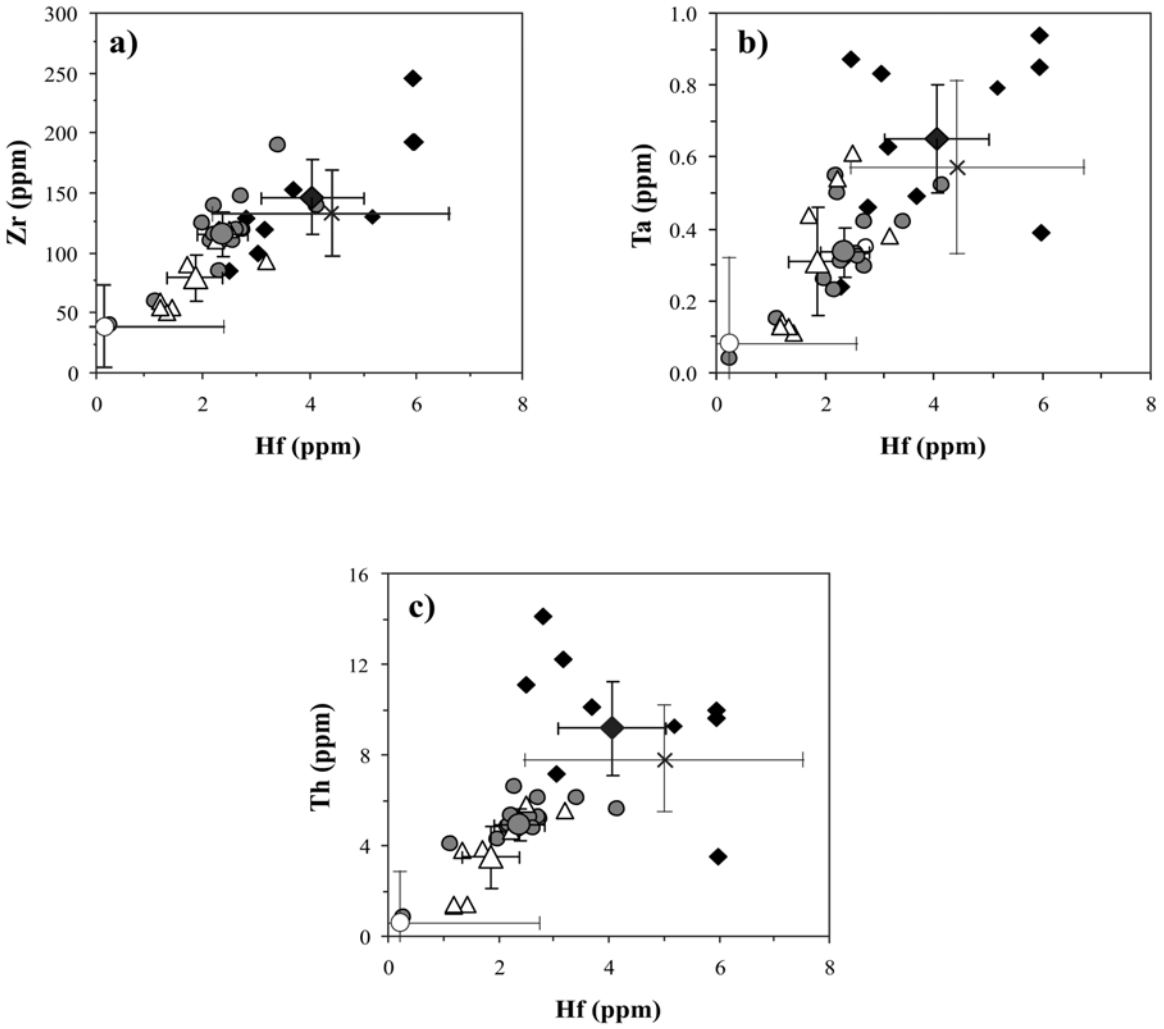

Fig. 11. Binary diagrams for abundances of selected high field strength elements (HFSE), for all suevitic, melt particle samples, and averaged compositions of suevitic groundmass (n = 8), bulk suevite (n = 15), melt particles (n = 10), SEMY (siliceous end-member for the Yax-1 impactites), and CEMY (carbonate end-member for the Yax-1 impactites) compositions of the Yax-1 impactite interval. Error bars represent 2σ standard deviations for the averaged compositions and least square y-estimate standard errors (Table 2) for the end-member compositions: a) Zr versus Hf; b) Ta versus Hf; c) Th versus Hf. Note the progressive enrichment of these HFSE towards the average melt particle composition.

Several melt particles are enriched in Ba (Table 4), having contents ranging from ~150 to 1280 ppm, compared to numerous samples having concentrations <150 ppm. Samples with relatively high Rb and Cs concentrations are exclusively from units 1 and 2 (Fig. 10a). When Rb + Cs, Sr, and Ba are compared against K + Na, no specific trends are evident, indicating that this effect is not controlled by specific alkali element-rich phases. However, when Rb + Cs values are plotted against FeO_{tot}, a rough correlation is observed (Fig. 10b). As with Rb and Cs, the enrichment of FeO_{tot} appears to be restricted to the upper impactite units (Table 4; also see Tuchscherer et al. 2004b). It is also observed that the greatest abundances of the LIL elements are held by the melt particle samples (Fig. 10b).

The high field strength elements (HFSE) Zr, Hf, Ta, Th, and U analyzed in this suite of impactites also have highly variable concentrations (Fig. 11; Table 5). Because of the incompatible behavior of these elements in silicate phases, plots of Ta, Zr, and Th versus Hf indicate positive linear correlations (Figs. 11a–c). When U concentrations are plotted against the other HFSE, inverse relationships are observed. With the exception of U, the melt particles are enriched in the HFSE, compared to the suevitic groundmass and bulk suevite (Table 5). The melt particles also have the largest compositional variability with regards to trace elements.

When plotted against Fe, the transition metals Sc, Co, and Zn give positive linear correlation trends (Figs. 12a–c), whereas Cr and Ni contents scatter (not shown). This behavior of Cr and Ni indicates that the distribution of a mafic component in the impactites is very heterogeneous. The

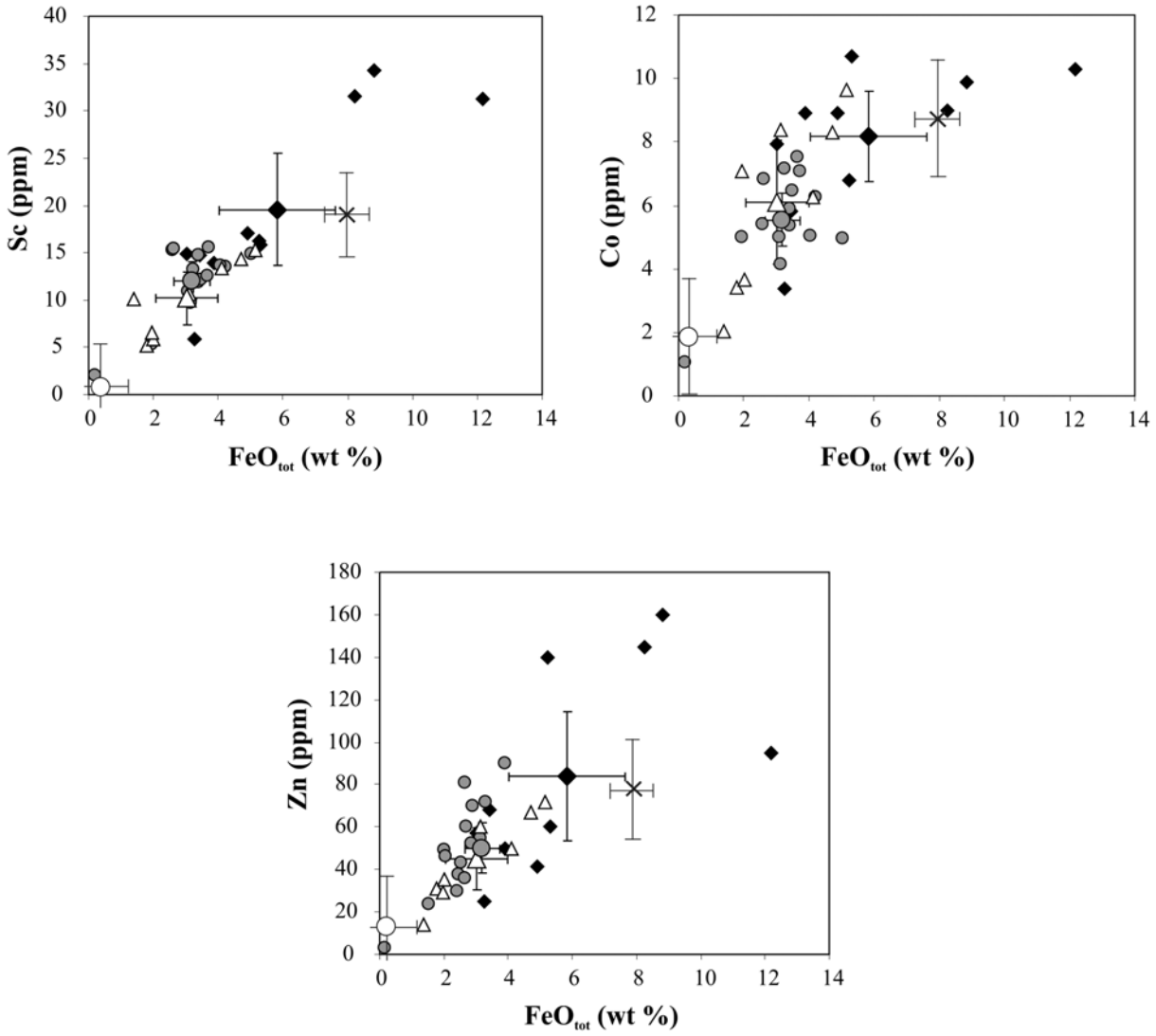

Fig. 12. Binary diagrams for selected transition trace metals versus FeO_{tot} showing all suevitic, melt particle samples, and averaged compositions for suevitic groundmass (n = 8), bulk suevite (n = 15), melt particles (n = 10), SEMY (siliceous end-member for the Yax-1 impactites) and CEMY (carbonate end-member for the Yax-1 impactites) of the Yax-1 impactite interval. Error bars represent 2σ standard deviations for averaged compositions (large symbols) and least square y-estimate standard errors (Table 2) for the end-member compositions: a) Sc versus Fe; b) Co versus Fe; c) Zn versus Fe. Note the relative enrichment of these selected elements against Fe toward the melt particle composition.

compositional variation and range of abundances of the transition metals are greatest for the melt particle suite.

Figure 13a shows that the heavy rare earth elements (HREE) for the SEMY of the Chicxulub impactites match the upper continental crust (UCC) (Taylor and McLennan 1985) composition well, whereas the light rare earth element abundances (LREE) are lower than those for the UCC composition. SEMY shares a negative Eu anomaly with the UCC. The CEMY and CTIY compositions are significantly depleted in the REE, in comparison with UCC and SEMY compositions. The carbonate end-member reveals a pronounced negative Ce anomaly. The averaged melt rock particles, bulk suevite, and suevitic groundmass all show normalized abundances that are a good match for the bulk continental crust (CC) composition, yet they are slightly enriched in LREE (Fig. 13b). The average melt particle, suevite, and groundmass compositions are very similar to, and intermediate between, the calculated SEMY and CEMY compositions (Fig. 13b). Among the lithic clasts (Fig. 13c), the gneissic sample reveals the highest REE normalized abundances, followed by those of the granodiorite and the dolomite. The dolomite has a pronounced negative Eu anomaly.

To compare compositional differences between the average impactite sample suites, clasts, and calculated end-members, the available data set has been normalized against

the composition of bulk CC and is compared against the trends for UCC and lower continental crust (LCC) (Fig. 14). Figure 14a shows that the calculated SEMY is primarily intermediate between the UCC and the bulk CC. An upper-crustal signature can be observed, as defined by the similar normalized abundances of K, Th, Hf, Zr, Sr, Na, Sb, Zn, Fe, Sc, Co, Cr, and Ni to those of the UCC. A complex pattern is defined by positive K, Th, Hf, and Zr, and negative U, Ba, Ta, and As anomalies. The lower crust, also shown in Fig. 14a, has considerably lower abundances of the alkali elements and HFSE, but is characteristically enriched in the transition metals. Figure 14b shows that the average for melt rock particles, the average bulk suevite, and average suevitic groundmass values produce relatively similar trends when normalized to the bulk CC, with the suevitic groundmass having the lowest normalized abundances. The average suevitic groundmass does not show a positive Th anomaly, but has a positive Sr anomaly. Figure 14c compares the compositions of the calculated CEMY and the dolomite clast with the bulk CC. The two phases have similar trends and overlapping abundances primarily below those of bulk CC. The trend is characterized by strong positive U, Sr, and Sb anomalies. The granodiorite clast (Fig. 14d) is strongly enriched in K, Ba, and, to a lesser extent, Zn compared to the gneissic clast. The gneiss shows only relative enrichments of K and Zr, and, to a lesser extent, of Th and Na, compared to the bulk CC. However, the high Th abundances observed in the SEMY and melt particle compositions are not characteristic for these clasts. Thus, a Th-rich target rock component is still to be identified. The SEMY and average melt particle compositions have Th values of 7.9 and 14.1 ppm, respectively. The highest Th content from a sampled clast originates from the finely laminated gneiss, at 4.5 ppm Th.

A pronounced negative As anomaly is observed when comparing the SEMY and all the impactite samples to the bulk CC (Figs. 14a and 14b). Bromine abundances of these samples (Table 4) (50–3 ppm) are unusually enriched when compared against the bulk CC (0.88 ppm, after Rudnick and Gao 2003). The chemical variation of impactites versus depth shows that, for Cs, Rb, Ni, Zn, Cr, and Sb, abundances are moderately enriched in the upper interval of the impactites, between 795 and 846 m depth (Fig. 2, Table 4). The samples from unit 5 yield the highest U and the lowest Cs, Rb, Hf, Zn, Sc, Cr, and Ni abundances. For a perspective on the carbonate content of the impactites, the HFSE, Sc and Hf, show low abundances in unit 5. Scandium and Hf are preferentially enriched in silicate phases. Thus, low concentrations of these elements indicate high carbonate abundances.

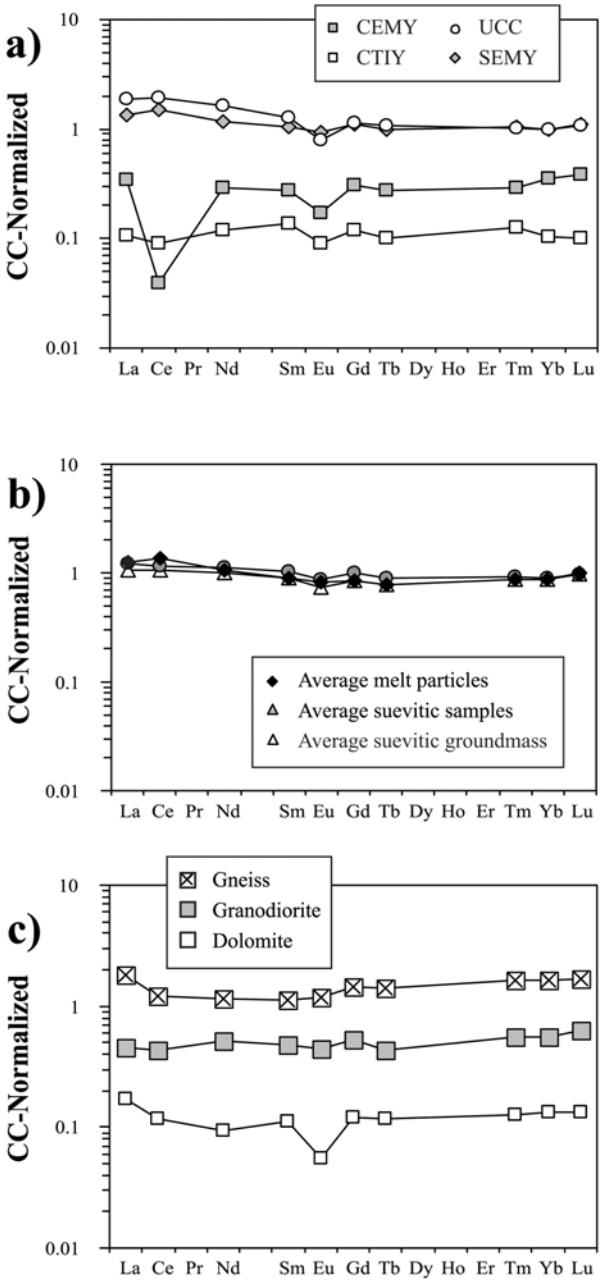

Fig. 13. Bulk continental crust (CC) normalized (values from Taylor and McLennan 1985) rare earth element (REE) patterns for a) upper continental crust (UCC), calculated siliceous (SEMY) and carbonate (CEMY) end-members for the Yax-1 impactites, and calculated average Cretaceous target rock interval composition of Yax-1 (CTIY); b) averaged suevitic groundmass (n = 8), bulk suevitic (n = 15), and melt rock samples (n = 10); c) individual clasts from the impactites: gneiss (824.03 m), granodiorite (88.92 m), and dolomite (888.09 m).

Geochemistry of Cretaceous Rocks

The results of major and trace element analyses for these lithologies are presented in Table 6. The average compositions for dolomite, argillaceous dolomite, and oil shale are presented in Table 7. The Cretaceous lithologies have high loss on ignition (LOI) values due to their high carbonate/sulfate contents and phyllosilicate presence. Silica and Al_2O_3 can also be quite elevated in certain samples, depending on the amounts of modal phyllosilicate. Oil shale

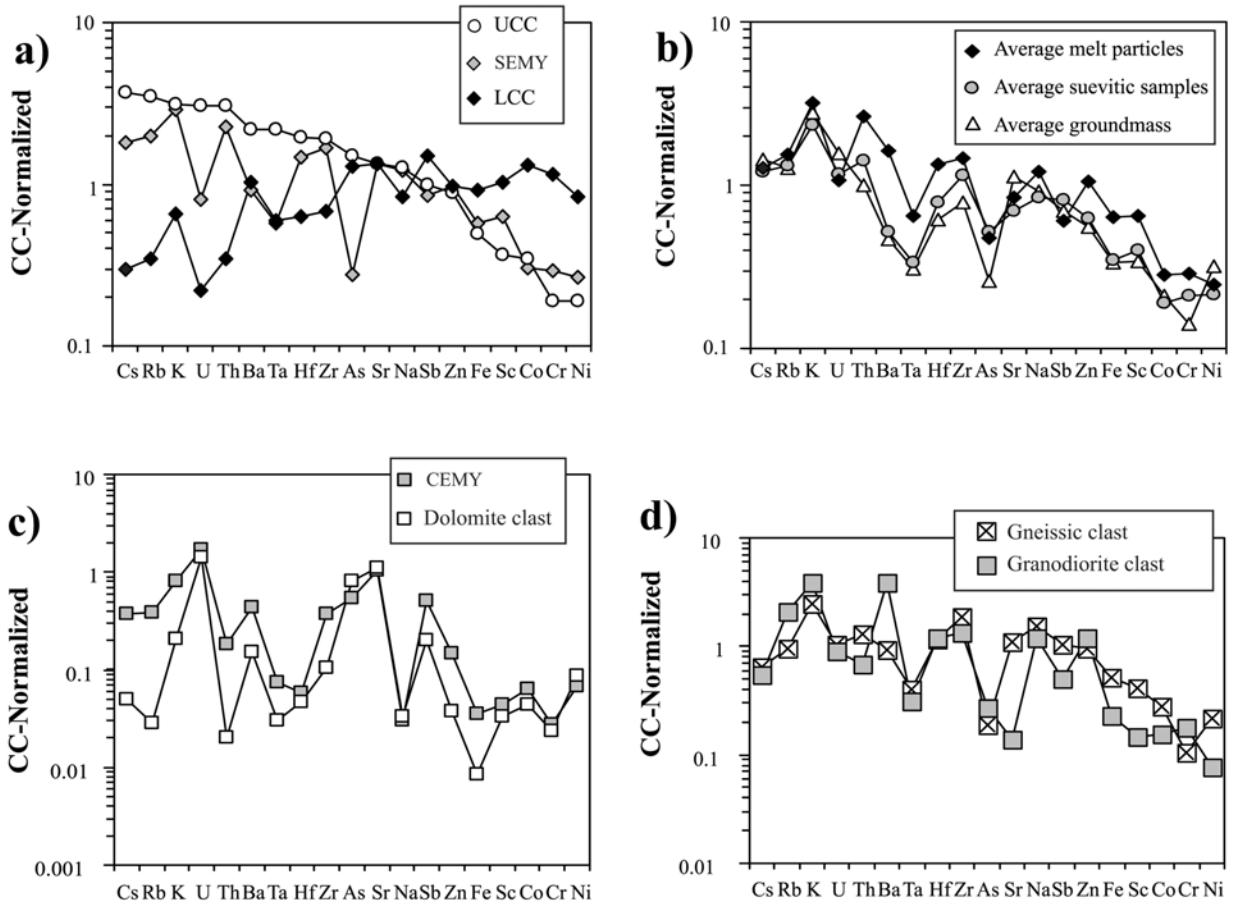

Fig. 14. Bulk continental crust (CC) normalized (values from Taylor and McLennan 1985) abundances of selected major elements, LIL elements, HFSE, volatile, and transition metals in impactites and clasts from the Yax-1 borehole. Elements are arranged according to their decreasing compatibility in the upper continental crust. a) Upper continental crust (UCC), calculated siliceous end-member of the Yax-1 impactite (SEMY), and lower continental crust (LCC); b) averaged melt particle composition, bulk suevite, and suevite groundmass; c) dolomite clast (depth = 888.09 m) and calculated carbonate end-member for the Yax-1 impactites (CEMY); d) siliceous crystalline clasts: granodiorite (depth = 888.92 m) and gneiss (depth = 824.03 m).

samples and, to a lesser extent, the argillaceous dolomite samples have high K_2O concentrations—higher than any impactite samples at up to 13.73 wt% K_2O (Table 6; Fig. 15a)—and relatively high Al_2O_3 and FeO_{tot} abundances. The blue, brecciated dolomite from 1347.56 m contains slightly higher K_2O than the other dolomite samples. The Na_2O content is quite low for all these samples. The MgO and SO_3 abundances calculated for the CTIY composition do not correlate with those of the CEMY calculated from the impactite compositions (Table 2), which is comparatively significantly enriched in CaO.

As with the impactites above, the analytical data for the Cretaceous samples have been normalized against the composition of bulk CC. Abundances for the LILE, HFSE, transition trace metals, and selected volatile elements are presented in order of decreasing compatibility with respect to UCC in Fig. 15. Lithologies have been grouped according to their similar geochemical signatures. Figure 15a shows that the average oil shale, argillaceous dolomite, and the alteration zone (see Table 7 for selected samples used in the averages) all have similar positive U, As, and Sb anomalies. The oil shale is highly enriched in these elements. The alteration zone is rich in Cs and Rb. In Fig. 15b, the calculated CTIY composition is plotted and shows similar chemical characteristics to the dolomite and anhydrite lithologies, obviously representing a mixture of these rocks. Compared to the rock types plotted in Fig. 15a, the CTIY composition, as well as the anhydrite and the evaporite, show similar chemical signatures but with significantly higher abundances of Sr, which is directly related to the anhydrite content. Analyses for several sandstones and a metaquartzite from the Y1 and Y4 boreholes, respectively (Koeberl 1993b), are presented for comparison in Fig. 15c, showing that these rocks are all rich in U, Th, Hf, Zr, As, and Sb. The volatile elements, As and Br, in the oil shale, argillaceous dolomite, the blue alteration zone, the evaporite (data from Koeberl 1993b), the average dolomite, and the CEMY are also strongly enriched when compared to the impactite samples and the bulk CC.

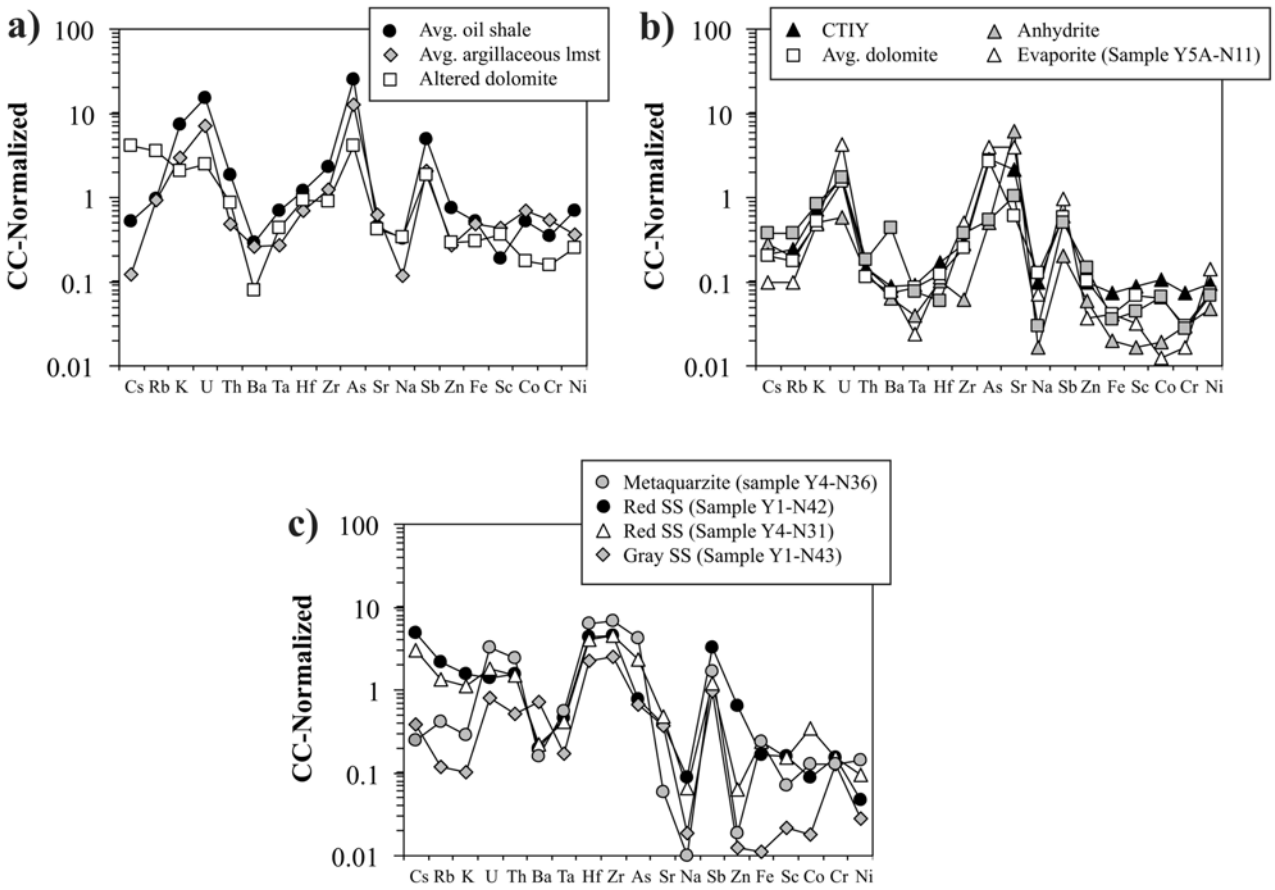

Fig. 15. Bulk continental crust (CC) normalized (values from Taylor and McLennan [1985]) data for major and LIL elements, HFSE, volatile elements, and transition metals in Yax-1 lithologies. Elements are arranged according to their decreasing compatibility in the upper continental crust. a) Average oil shale (n = 3), average argillaceous limestone (n = 4), and alteration zone sample from 1347.60 m. b) Yax-1 aggregate Cretaceous target composition (CTIY), average Yax-1 dolomite (n = 15), anhydrite, and evaporite data (the latter after Koeberl 1993). c) Clastic sedimentary rocks metaquartzite, red sandstone (SS), and grey SS, after data by Koeberl (1993).

The average oil shale and average argillaceous dolomite show similar rare earth element abundances trends, with pronounced negative Ce and positive Sm anomalies (Fig. 16a). The alteration zone, however, is relatively enriched in light rare earth element abundances and shows a pattern that is similar to that of average dolomite (Fig. 16b). This illustrates also that the calculated CTIY composition is almost identical to the average dolomite pattern, with respect to REE systematics, despite 27.4 vol% anhydrite in the calculated CTIY composition contains. The anhydrite sample No. 233A has the lowest REE-normalized abundances, compared also to the evaporite sample (Y5A-N11, from borehole Y5) of Koeberl (1993b). This latter analysis most likely represents a mixture of argillaceous limestone and/or oil shale with anhydrite, as it shows characteristic negative Ce and Eu, and positive Sm anomalies (Fig. 16a), as well as relatively high Sr abundance (Fig. 16b). In general, all dolomite samples are characterized by a negative Ce anomaly. The clastic sediments (Fig. 16c) all show similar REE trends at distinctly variable abundances.

DISCUSSION

Compositions of End-Member Components of Yax-1 Impactites

Siliceous End-Member

When the siliceous end-member (SEMY) composition is compared to the averaged melt rock particle composition (Figs. 13 and 14), nearly identical patterns are observed. The only significant differences are that the average melt particle composition has a lower Sr but a higher Ba content than SEMY. SEMY has an REE geochemical signature that is similar to that of the UCC. This is obvious on a bulk continental crust (CC)-normalized REE diagram (Fig. 13a) where the HREE pattern is identical to that of the upper continental crust (UCC) and the LREE are only slightly depleted. The spider diagram of Fig. 14a shows that K, Th, Hf, Zr, Sr, Na, Sb, Zn, Fe, Co, Cr, and Ni of the SEMY composition have abundances that are nearly identical to those of the UCC. On the other hand, Cs, Rb, U, Ta, and As

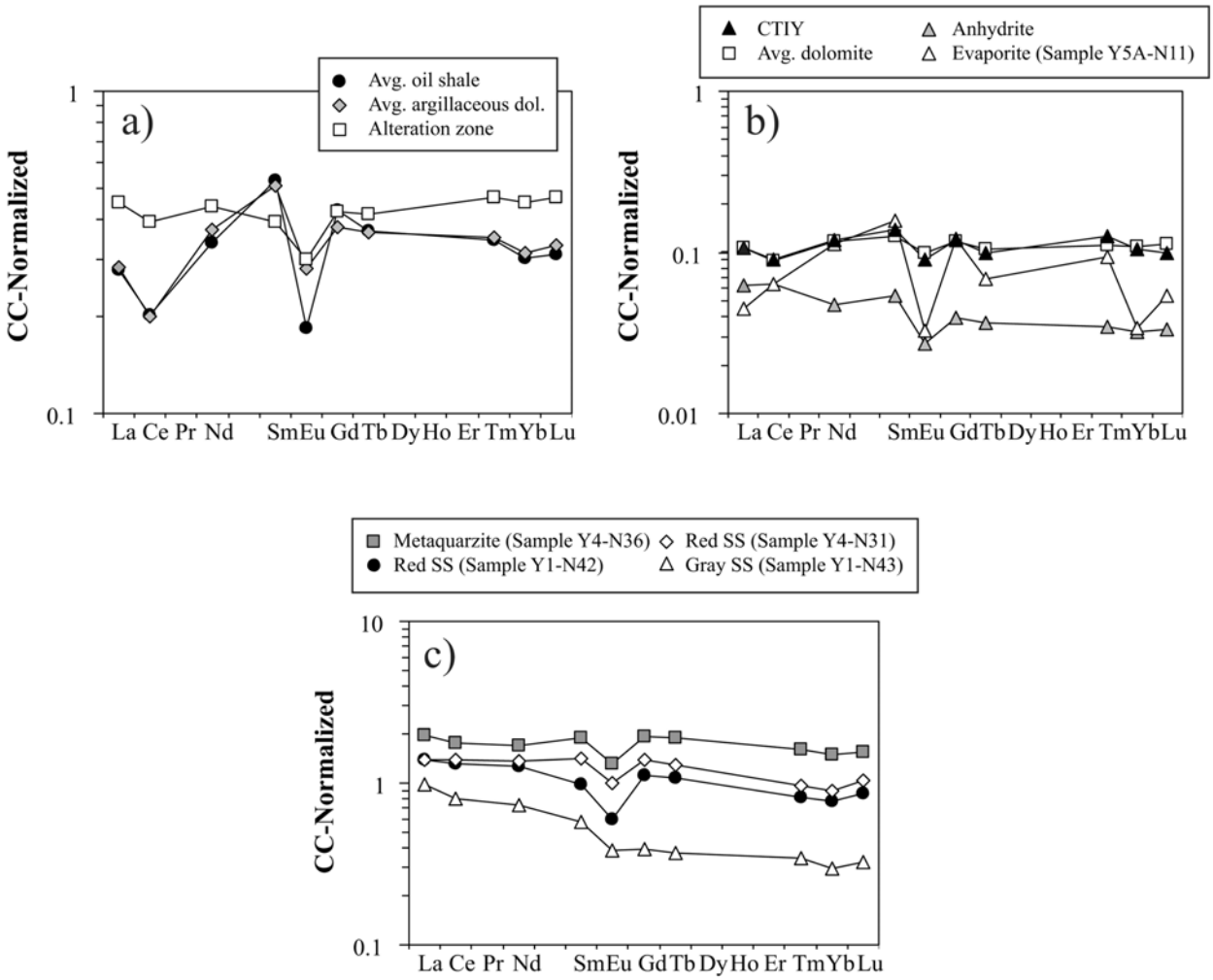

Fig. 16. Bulk continental crust (CC) normalized (values from Taylor and McLennan [1985]) REE abundances for: a) Average oil shale (n = 3), average argillaceous limestone (n = 4), and the alteration zone sample from a depth of 1347.60 m. b) Yax-1 aggregate Cretaceous rock composition (CTIY), average Yax-1 dolomite (n = 15), anhydrite, and evaporite compositions (the latter from Koeberl 1993). c) Clastic sedimentary rocks (metaquartzite, red sandstone (SS), and grey SS) from Koeberl (1993).

have abundances that are significantly more variable and intermediate between those of the UCC and the bulk CC. These results show that the crust struck by the Chicxulub impactor was deficient in Cs, Rb, and Ta, but slightly enriched in Sc, Cr, and Ni.

The discrepancy between the impactite composition and the UCC can be explained by a variety of processes. A high loss on ignition (LOI) value is evident from the major element composition; this affects the bulk silicate composition. High LOI is attributed to the high secondary and clastic carbonate contents of the impactites. Alteration has also resulted in extensive conversion of melt particles into phyllosilicates, with accompanying change of the composition of the bulk impactite material.

High LOI of impact crater fill must be expected to result from a wet impact, i.e., hydrous target rocks and interaction with seawater. A minor positive Ce anomaly is noted for SEMY, which indicates strong interaction with seawater. This may occur through the preferential microbially mediated oxidation of dissolved Ce^{3+} to the insoluble form Ce^{4+} in seawater. The anomaly is believed to originate from the enrichment of insoluble Ce^{4+} in residual authigenic minerals, i.e., clay minerals and Ca phosphates (e.g., Guy et al. 1999; Utzmann et al. 2002). Even if the major element abundances are recalculated on a LOI-free basis, the resultant composition does not equate to that of the UCC, having relatively lower SiO_2 (58.05 wt%) and higher CaO (5.74 wt%) contents. SEMY was calculated assuming a CaO content of 5.2 wt%, which is identical to the CaO content of unit 4 (Tuchscherer et al. 2004b) and previously reported compositions of the Yucatán crystalline basement (e.g., Kring 1997). This CaO content is slightly higher than that of the average UCC, i.e., 4.2 wt% (Taylor and McLennan 1985), which might be influenced by the incorporation of lime from the target

carbonate rocks. Secondary processes have thus had a strong influence on the present composition of the impactite.

Based on the calculated SEMY composition, we suggest that the crust struck by the Chicxulub impactor was more mafic than the UCC estimate of Taylor and McLennan (1985). In agreement with this finding, a significant mafic target rock component to the Chicxulub impactite has been invoked by Kettrup et al. (2000) in order to explain their Sr and Nd isotope data. Our petrographic findings (Tuchscherer et al. 2004a) include observation of some clasts of mafic rocks (gabbroic and mica schist clasts) throughout the impactite interval, albeit in very small volume percentages (i.e., total clastic content, siliceous and mafic <<2.5 vol%). Furthermore, abundant altered mafic melt rock particles have been found in the Yax-1 suevites (Tuchscherer et al. 2004a).

Carbonate End-Member

The carbonate end member (CEMY) for the impactites of the Yax-1 borehole has a trace element geochemical signature that differs slightly from that of the calculated Cretaceous target rock interval in Yax-1 (CTIY). Figure 13a shows that the calculated CEMY has a normalized REE pattern that is almost identical to that of the CTIY composition, but with pronounced negative Ce and Eu anomalies. According to Elderfield et al. (1981), the negative Ce anomaly is a characteristic of seawater-precipitated sedimentary rocks and minerals, e.g., limestone, dolomite, and anhydrite (cf. Figs. 16a and 16b). With regard to the normalized trace element patterns (Fig. 14c), the pattern for the CEMY overlaps with that for a dolomite clast in the impactite. The average dolomite composition shows similar peaks of U, As, and Sb, but with lower Ba and Sr (Fig. 15b). The high Ba and Sr in the CEMY can be attributed to the presence of authigenic barite, which indeed has been observed abundantly by several groups, e.g., Hecht et al. (2004) and Tuchscherer et al. (2004a). The calculated CTIY, plotted on a similar multi-element diagram (Fig. 15b), is slightly different from that of the CEMY, showing a pronounced positive As anomaly and relatively higher U and Sr normalized abundances. The differences in the calculated CTIY composition and that of the CEMY can be attributed to an incomplete record of Cretaceous, and possibly older, lithologies of the target volume that was sampled by the Yax-1 borehole (e.g., the borehole did not intersect any clastic sedimentary rocks), to the devolatilization of anhydrite and other highly volatile phases (e.g., As) during the impact event (as postulated by, e.g., Sigurdsson et al. 1992 or Ivanov et al. 1996), and to the presence of quite a significant amount of calcite and barite in the impactites.

Petrographic observations have demonstrated that numerous secondary calcite veins with barite crystals occur in the impactite interval, in particular in units 3 and 4 (Hecht et al. 2004; Tuchscherer et al. 2004a). With regards to the devolatilization of anhydrite, Ames et al. (2004), Schmitt et al. (2004), and Tuchscherer et al. (2004b) have demonstrated that the Yax-1 impactites have very low sulfate (from <0.02 to 0.15 wt% SO_3). This has also been observed in the impactites of the Y6 drill core (Claeys et al. 2003). This effect is also obvious when the sulfate abundance of the calculated carbonate end-member is compared with the calculated Cretaceous target rock composition (Table 7).

From the calculated compositions of CTIY, it is also noted that CEMY is more calcitic than expected on the basis of the prominence of dolomite in the Cretaceous stratigraphy (Table 7). This can be explained in several ways: 1) Pervasive secondary calcite has entered the impactites in significant proportion. 2) Our calculated CTIY composition does not adequately represent the bulk Cretaceous (and older) carbonate rocks at Chicxulub, i.e., a more limestone-rich, rather than dolomitic target rock component was incorporated into the Yax-1 impactites. 3) Lime may have preferentially been taken up into the impactites compared to MgO (in dolomite) due to the fast back-reaction of CO_2 with CaO and the comparatively poor reactivity of MgO (Agrinier et al. 2001). MgO does not appear to have been preferentially incorporated into the impactites as both the SEMY and the CEMY do not show substantial concentrations of MgO (4.23 and 5.51 wt%, respectively) compared to the CTIY (13.62 wt%). The unusual and unique MgO-rich composition of magnesiowüstite spinels found in K/T boundary ejecta of the Pacific Ocean region compared to all other K/T boundaries (Kyte et al. 1996; Ebel and Grossman 2005) may account for some of this missing MgO.

Comparisons of Suevitic Groundmass and Bulk Suevite

The average suevitic groundmass and average bulk suevite compositions are similar (Table 5; Figs. 9a, 9b, 10b, 11a–c, 12a–c, and 14b) and clearly contain similar proportions of silica-rich and carbonate components. In the case of bulk suevite, these components are primarily melt particles and suevitic groundmass. In the suevitic groundmass, the principal components are calcite, dolomite, microscopic melt particles, lithic clasts, and an altered alkali element-, Ca-, and Si-rich cement (Tuchscherer et al. 2004a). The lithic clasts and melt particles, in both bulk suevite and suevitic groundmass, have been extensively converted to phyllosilicates (cf. Tuchscherer et al. 2004a).

The average groundmass composition is enriched in Sr and the average suevite in Th. The Sr could originate from anhydrite preserved in the groundmass (Figs. 14b and 15b) or the presence of Sr-rich barite (Hecht et al. 2004). Conversely, the positive Th anomaly observed in the average suevite composition could originate from melt particles that were originally clastic sedimentary rocks (Lopez Ramos 1975; Koeberl 1993b; Ward et al. 1993) or as yet unsampled granitoid lithologies.

Melt Particle Compositions

Melt particles have variable chemical compositions (Tables 4 and 5; Figs. 9a, 9b, 10b, 11a–c, 12a–c, and 14b) (Tuchscherer et al. 2004a). Among the 10 newly analyzed individual melt particle compositions, several geochemical groupings can be discerned. The gray melt particle samples 755A, 755AD, 769C, and 770B (Table 4) show high Zn, Fe, and Hf concentrations. This group is also distinguished by its overall low element abundances of certain elements, especially of K and Th, which do not exceed three times the bulk CC values. This group of melt particles is similar to the type 4 melt particles identified by Hecht et al. (2004) based on the low K content and their opaque petrographic characteristics. The second group of melt particles has high Ba and low Ta concentrations and includes the samples 752A, 769C, 756, 241, and 225B (Table 4). Based on these data, these samples could represent melted granodiorite, which also contains high Ba and low Ta (Table 4; Fig. 14d). However, these groupings are not entirely separated compositionally. For example, sample 769C shows characteristics from both groups. Because the second melt particle population possesses variable textural attributes, such as variegated colors and fluidal to shard-like morphologies, we cannot correlate these samples with any of the groups defined by Hecht et al. (2004).

The difficulty of trying to decipher the protolith composition of melt particles stems from the fact that the Chicxulub situation includes impact-induced mixing as well as alteration of different degrees (i.e., open system behavior), and the samples are diluted by secondary carbonate. To further investigate potential protolith compositions of melt particles, element ratios—especially those involving immobile HFSE, e.g., Zr/Hf and Hf/Ta ratios—were applied. From Tables 4 and 6, and data from Koeberl et al. (1993), it is seen that the currently known target rock compositions have Hf/Ta ratios that only bracket the upper range of the melt particle composition. When considering Zr/Hf ratios, the melt particles produce unusually low ratios that cannot be accounted for by any currently known siliceous target rock. Other means are thus required in order to discern the protolith composition(s) of melt rock particles. The lack of geochemical data from any mafic target lithology prohibits any mixing calculations, at this stage.

Cretaceous Rock Geochemistry: Implications

Certain aspects of the geochemical results for Cretaceous lithologies merit further discussion. Most Cretaceous rocks, i.e., the oil shale, average argillaceous limestone, average dolomite, evaporite (from Koeberl 1993b), and a few clastic, silicate-rich, sedimentary rocks (samples Y4-N36, Y4-N31 from Koeberl 1993b) have relatively high U abundances compared to the bulk CC (Fig. 15). The U contents, as well as the K and Th contents, of these rocks are well documented in the downhole gamma ray log for Yax-1 (Kenkmann et al. 2004; Wohlgemuth et al. 2004). The high U abundances may be explained by either a high U provenance for these sedimentary deposits or the preferential affinity of U toward organic matter in sedimentary rocks, preserved in the form of stable organo-uranyl compounds during diagenesis (e.g., Nakashima et al. 1984). This most likely occurs through the transport of highly soluble $[UO_2]^{2-}$ ions (McLennan and Taylor 1980). Our single sample of Tertiary limestone and the North American Shale Composite (NASC) (Gromet et al. 1984), however, do not show anomalous U abundances when normalized to bulk CC. This may indicate that high U concentrations are typical of the Cretaceous target rocks. Unit 5 impactites have the highest U abundances, and, thus, record a strong Cretaceous rock component.

Potassium abundances sampled in oil shale horizons in the Yax-1 borehole are anomalously high (Tables 6 and 7). Increased illitization, i.e., increased K content, with depth, in carbonate rocks associated with a major oil-producing basin, has been recently documented by Iftikhar et al. (2004) from the Hibernia oil field off the coast of Newfoundland, Canada. These authors suggested that the illitization occurred as the result of K-rich fluids migrating along fault zones, which were also exploited by migrating hydrocarbons. This study suggests that such pathways may occur in the form of our sampled oil-shale horizons (Fig. 8). As the oil shales occur below 1500 m in the Yax-1 borehole, this depth interval appears to be consistent with the onset of catagenesis in oil-producing carbonate rocks (Tissot and Welte 1978).

The altered rock located at 1347–1348 m appears to coincide with slightly elevated K and U gamma ray intensities (Kenkmann et al. 2004). Whole-rock analyses (Table 6) (Schmitt et al. 2004) indicate this rock contains high SiO_2, Al_2O_3, K_2O, and Na_2O abundances, and the abundances for the trace elements Sc, Cr, Co, Ni, Zn, Rb, Zr, Sb, Cs, REE, Th, and U are also elevated in comparison to the host dolomitic rocks (Fig. 15b). The alteration zone displays a similar trace element profile and abundances to the average argillaceous dolomite and average oil shale, but has higher Cs and Rb (Fig. 15a). The REE, however, are not similar to the average argillaceous dolomite and average oil shale; they are LREE-enriched. Considering our inability to identify bona fide shock metamorphic characteristics in this interval, an endogenic origin as part of the target sequence is thus more likely for this rock type, i.e., an illite-rich dolomitic rock (see next section).

Cretaceous Rocks: Impact-Induced Deformation?

Several Cretaceous rock samples from between 1315 and 1399 m in the Yax-1 borehole have distinct deformation features in the form of extensive brittle fractures and breccias. This deformation evidence must be discussed with regard to

impact versus endogenic deformation. The brittle deformation fractures (Figs. 3i, 5, and 6) were probably produced by the Chicxulub impact event. As also suggested by Kenkmann et al. (2004), brittle deformation appears to be lithologically controlled, being more dominant in the dolomitic rocks (Figs. 5, 6, and 8) than in anhydrite and argillaceous dolomites. Several breccia horizons are found in the Cretaceous rocks, which indicate extensive faulting with pervasive fragmentation (Figs. 5 and 6). However, the paucity of shock metamorphic deformation effects in the limited amount of silicate minerals, due to the carbonate-dominated composition of the target rocks, makes the correlation of this deformation with the Chicxulub impact difficult (Kenkmann et al. 2004).

The extensive fracturing that characterizes the polymict breccia (Fig. 6) is difficult to reconcile with typical dissolution of carbonate/sulfate, as extensive translation is required to produce such a fault. Even if the dissolution of carbonate/sulfates had produced the brittle deformation observed in the dolomite, a later extensive deformation event would have to be invoked in order to explain the formation of this rather thick polymict breccia horizon. Based on these arguments, the formation of this polymict breccia is most likely the result of the Chicxulub impact event.

Other petrographic criteria were defined by Kenkmann et al. (2004) in order to link the observed deformation with the impact, i.e., the identification of fine-grained, low-porosity faults atypical of solution collapse produced in an extensional regime. Kenkmann et al. (2004) showed that the displacement to thickness (D/T) ratio of the brittle fault zones is not typical of tectonic shear zones but that the thickness of some of these faults indicates "dynamic shock loading before shear zone formation." Most of the faults in the dolomite are indicative of "oscillating" conditions atypical of the incremental nature of endogenic faults, as no visible offset is observed (Kenkmann et al. 2004). Thus, we believe, in conjunction with our observations of brittle fractures, that the extensive fracture pattern observed in Yax-1 Cretaceous dolomitic rocks (Figs. 2 and 5) is most likely a product of the energy transfer that occurred immediately after impact.

In keeping with the observations by Kenkmann et al. (2004) and Wittmann et al. (2004), we have not found any bona fide shock metamorphic silicate mineral deformation or impact melt particles in our samples from the 1314 to 1399 m interval. This also refers to the so-called "impact melt rock" samples described by these authors from the interval between 1347 and 1348 m (Table 3). Bona fide PDFs and melt particles have been identified in the suevitic dikes at 909 and 916 m depths, and PDFs alone in the meta-paraconglomerate at 1036 m (also described by Kenkmann et al. 2004). Stinnesbeck et al. (2004) also indicated that they had not found evidence for impact-induced deformation of the Cretaceous target rocks (they referred to overturned bedding, steeply dipping lithologies, major mechanical fragmentation, and shock metamorphism). These authors suggested that the observed deformation was more likely the result of intraformational processes, i.e., the "dissolution of evaporites." We do not agree with Stinnesbeck et al. (2004) that the observed deformation in the Cretaceous rocks is primarily a product of dissolution. We suggest the Cretaceous rocks record a multistage history of deformation that encompasses impact-induced brittle deformation that overprints traditional dissolution-related carbonate deformation, i.e., dissolution related anhydrite is crosscut by a monomictic breccia dike at 1314.83 m (sample 233) and brittle fractures crosscutting stylolites observed in the 1347–1348 m interval (Fig. 7).

The location of the Yax-1 borehole with respect to the crater center and the associated attenuated shock wave have to be considered in order to provide insight into the formation of shock deformation features and melt production. Because the Yax-1 borehole is located at quite a distance from the crater center, it might not have been subjected to the significant shock levels required to locally produce characteristic (e.g., PDFs) shock microdeformation or impact melt. Already at >10 km radial distance downrange from the crater center, shock levels have been estimated by numerical modelling at less than 10 GPa, for impact angles between 90° and 45° (Pierazzo and Melosh 1999), the minimum shock pressure required for planar deformation feature (PDF) formation (e.g., French 1998). Furthermore, at a distance of 60 km from the center of the Sudbury impact crater, shock levels, also determined by numerical modelling, were shown to be <10 GPa (Ivanov and Deutsch 1999), and at 20 km from the heavily eroded center of the Vredefort impact crater of South Africa, shock levels have been recorded to be <10 GPa (Gibson and Reimold 2005). These numerical and field studies agree with our observation regarding the paucity of shock-related microdeformation features such as PDFs in the clastic Cretaceous components (Tuchscherer et al. 2004a) and on the endogenic origin of the altered dolomitic breccia interval between 1347 and 1348 m. We suggest this horizon was likely a section of intense dissolution.

CONCLUSIONS

1. Melt particles in Yax-1 impactites represent mixtures of various siliceous target rocks. Therefore, the use of element ratios cannot constrain the melt particle precursor compositions. This is also hindered by the paucity of analyzed mafic target rocks.
2. The average bulk suevite and suevitic groundmass compositions are similar to each other and thus must be composed of similar proportions of precursor components. Minor siliceous and carbonate target rock geochemical characteristics can be observed in the suevite and groundmass, respectively.

3. The siliceous end-member of the Yax-1 impactites has a trace element signature that is similar to that of the upper continental crust, i.e., it has similar abundances of Sr, Na, Sb, Zn, Fe, Co, Cr, Ni. When the siliceous end-member composition is calculated on a LOI-free basis, a significant mafic component becomes apparent in the Yucatán target volume.
4. The calculated carbonate end-member of the Yax-1 impactites indicates that the impactites are anomalously rich in calcite when compared to the calculated Cretaceous target rock composition. This indicates that our estimate of the Cretaceous target rock composition is either not a true representation of the Cretaceous rocks, and/or secondary calcite occurs in proportions great enough to significantly alter the carbonate end-member composition. The trace element signature of the carbonate end-member indicates that dolomitic rocks must have been a major component in the impactites and that U is a ubiquitous component.
5. Deformation features observed in the investigated interval between 1315 and 1399 m of the Cretaceous target rock indicate a multistage deformation history from pre- to post-impact times. A detailed microscopic investigation did not document any characteristic shock-related deformation microfeatures. This makes the correlation of deformation features with the Chicxulub impact difficult. However, using crosscutting relationships between the target rocks and brecciated intervals, at least one episode of deformation can be constrained that must be related to the Chicxulub impact.
6. We find no conclusive evidence that would suggest the brecciated interval between 1347 and 1348 m is an impact melt breccia. Mineralogical and textural indicators are more consistent with this breccia being interpreted as an alteration horizon that underwent extensive dissolution through the migration of K-rich fluids associated to brine reflux. The occurrence of oil-bearing shale below this impermeable horizon is also consistent with the onset of catagenesis, i.e., the oil-window. High concentrations of K were found in the oil-shale, which indicates that these layers may have been adequate pathways for the migration of fluids and hydrocarbons.

Acknowledgments–All of the authors gratefully acknowledge the comprehensive financial support that this project has received from a Petroleum Research Fund grant (PRF #37299-AC8) from the American Chemical Society. Detailed reviews by Phillip Claeys and Ralf Schmitt, and input from Ulrich Riller have significantly improved the manuscript. Thanks are also due to Maria Anastova at the Council for Geosciences (Pretoria), who provided valuable support with the SEM investigations. C. Koeberl's work was funded by the Austrian Science Foundation project P17194-N10. This is University of the Witwatersrand Impact Cratering Research Group Contribution No. 94.

Editorial Handling—Dr. Ulrich Riller

REFERENCES

Agrinier P., Deutsch A., Schärer U., and Martinez I. 2001. Fast back-reactions of shock-released CO_2 from carbonates: An experimental approach. *Geochimica et Cosmochimica Acta* 65: 2615–2632.

Ames D. E., Kjarsgaard I., Pope K. O., Dressler B., and Pilkington M. 2004. Secondary alteration of the impactite and mineralization in the basal Tertiary sequence, Yaxcopoil-1, Chicxulub impact crater, Mexico. *Meteoritics & Planetary Science* 39:1145–1167.

Blum J. D., Chamberlain C. P., Hingston M. P., Koeberl C., Marin L. E., Schuraytz B. C., and Sharpton V. L. 1993. Isotopic comparison of K/T boundary impact glass with melt rock from the Chicxulub and Manson impact structures. *Nature* 364:325–327.

Butler I. B. and Rickard D. 2000. Framboidal pyrite formation via the oxidation of iron (II) monosulfide by hydrogen sulphide. *Geochimica et Cosmochimica Acta* 64:2665–2672.

Claeys P., Heuschkel S., Lounejeva-Baturina E., Sanchez-Rubio G., and Stöffler D. 2003. The suevite of drill hole Yucatán 6 in the Chicxulub impact crater. *Meteoritics & Planetary Science* 38: 1299–1317.

Combaz A. 1970. Microsphérule muriforms dans les roches mères du pétrole, hypothèse sur leur origine. *Comptes Rendus Académie des Sciences (Paris) Série D* 270:2240–2243.

Dressler B. O., Sharpton V. L., Morgan J., Buffler R., Moran D., Smit J., Stöffler D., and Urrutia-Fucugauchi J. 2003. Investigating a 65-Ma-old smoking gun: Deep drilling of the Chicxulub impact structure. *EOS* 84:125–131.

Dressler B. O., Sharpton V. L., Schwandt C. S., and Ames D. 2004. Impactites of the Yaxcopoil-1 drilling site, Chicxulub impact structure: Petrography, geochemistry, and depositional environment. *Meteoritics & Planetary Science* 39:857–878.

Ebel D. and Grossman L. 2005. Spinel-bearing spherules condensed from the Chicxulub impact-vapor plume. *Geology* 33:293–296.

Elderfield H., Hawkensworth C. J., Greaves M. J., and Calvert S. E. 1981. Rare earth element geochemistry of oceanic ferromanganese nodules and associated sediments. *Geochimica et Cosmochimica Acta* 45:513–528.

French B. M. 1998. *Traces of catastrophe: A handbook of shock-metamorphic effects in terrestrial meteorite impact structures*. Houston: Lunar and Planetary Institute. 120 p.

Gibson R. L. and Reimold W. U. 2005. Shock pressure distribution in the Vredefort impact structure, South Africa. In *Large meteorite impacts III*, edited by Kenkmann T., Hörz F., and Deutsch A. Special Paper #384. Boulder, Colorado: Geological Society of America. pp. 329–349.

Guy C., Daux V., and Schott J. 1999. Behaviour of rare earth elements during seawater/basalt interactions in the Mururoa Massif. *Chemical Geology* 158:21–35.

Gregg J. M. and Sibley D. F. 1984. Epigenetic dolomitization the origin of xenotopic dolomite texture. *Journal of Sedimentary Petrology* 54:907–931.

Grieve R. A. F. and Therriault A. M. 2000. Vredefort, Sudbury, Chicxulub: Three of a kind? *Annual Reviews in Earth and Planetary Science* 28:305–338.

Gromet L. P., Dymek R. F., Haskin L. A., and Korotev R. L. 1984.

The "North American Shale Composite": Its compilation, major and trace element characteristics. *Geochimica et Cosmochimica Acta* 48:2469–2482.

Hecht L., Wittman A., Schmitt R. T., and Stöffler D. 2004. Composition of impact melt particles and the effects of post-impact alteration in suevitic rocks at the Yaxcopoil-1 drill core, Chicxulub crater, Mexico. *Meteoritics & Planetary Science* 39: 1169–1186.

Hildebrand A. R., Penfield G. T., Kring D., Pilkington M., Camargo A., Jacobsen S. B., and Boynton W. 1991. Chicxulub Crater: A possible Cretaceous-Tertiary boundary impact crater on the Yucatán peninsula, Mexico. *Geology* 19:867–871.

Iftikhar A. A., Hesse R., and Harper J. D. 2004. Variations in mixed-layer illite/smectite diagenesis in the rift and post-rift sediments of the Jeanne d'Arc Basin, Grand Banks offshore Newfoundland, Canada. *Canadian Journal of Earth Science* 41:401–429.

Ivanov B. A., Badjukov O. I., Yakovlev M. I., Gerasimov M. V., Dikov Yu. P., Pope K. O., Ocampo A. C. 1996. Degassing of sedimentary rocks due to Chicxulub impact: Hydrocode and physical simulations. In *The Cretaceous-Tertiary event and other catastrophes in Earth history*, edited by Ryder G., Fastovsky D., and Gartner S. GSA Special Paper #307. Boulder, Colorado: Geological Society of America. pp. 125–139.

Ivanov B. A. and Deutsch A. 1999. Sudbury impact event: Cratering mechanics and thermal history. In *Large meteorite impacts and planetary evolution II*, edited by Dressler B. O. and Sharpton V. L. GSA Special Paper #339. Boulder, Colorado: Geological Society of America. pp. 389–397.

Jercinovic M. J., Keil K., Smith M. R., and Schmitt R. A. 1990. Alteration of basaltic glasses from north-central British Columbia, Canada. *Geochimica et Cosmochimica Acta* 54:2679–2696.

Kenkmann T. 2002. Folding within seconds. *Geology* 30:231–234.

Kenkmann T., Wittmann A., and Scherler D. 2004. Structure and impact indicators of the Cretaceous sequence of the ICDP drill core Yaxcopoil-1, Chicxulub impact crater, Mexico. *Meteoritics & Planetary Science* 39:1069–1088.

Kettrup B., Deutsch A., Ostermann M., and Agrinier P. 2000. Chicxulub impactites: Geochemical clues to the precursor rocks. *Meteoritics & Planetary Science* 35:1229–1238.

Koeberl C. 1993a. Instrumental neutron activation analysis of geochemical and cosmochemical samples: A fast and reliable method for small sample analysis. *Journal of Radioanalytical and Nuclear Chemistry* 168:47–60.

Koeberl C. 1993b. Chicxulub crater, Yucatán: Tektites, impact glasses, and the geochemistry of target rocks and breccias. *Geology* 21:211–214.

Koeberl C. and MacLeod K. G., editors. 2002. *Catastrophic events and mass extinctions: Impacts and beyond*. GSA Special Paper #356. Boulder, Colorado: Geological Society of America. 746 p.

Kring D. A. 1997. Composition of Earth's continental crust as inferred from the compositions of impact melt sheets (abstract #1084). 28th Lunar and Planetary Science Conference. CD-ROM.

Kring D. A., Hörz F., Zurcher L., and Urrutia Fucugauchi J. 2004. Impact lithologies and their emplacement in the Chicxulub impact crater: Initial results from the Chicxulub Scientific Drilling Project, Yaxcopoil-1, Mexico. *Meteoritics & Planetary Science* 39:879–897.

Kyte F. T., Bostwick J. A., and Zhou L. 1996. The Cretaceous-Tertiary boundary on the Pacific plate: Composition and distribution of impact debris. In *The Cretaceous-Tertiary event and other catastrophes in Earth history*, edited by Ryder G., Fastovsky D., and Gartner S. Special Paper #307. Boulder, Colorado: Geological Society of America. pp. 389–401.

Lopez-Ramos E. 1975. Geological summary of the Yucatán Peninsula. In *The ocean basins and margins: The Gulf of Mexico and the Caribbean*, vol. 3, edited by Nairn A. E. M. and Stehli F. G. New York: Plenum Press. pp. 257–282.

McLennan S. M. and Taylor S. R. 1980. Th and U in sedimentary rocks: Crustal evolution and sediment recycling. *Nature* 285: 621–624.

Morgan J., Warner M., Brittan J., Buffler R., Camargo A., Christeson G., Denton P., Hildebrand A., Hobbs R., MacIntyre H., MacKenzie G., Maguire P., Marin L., Nakamura Y., Pilkington M., Sharpton V. L., Snyder D., Suarez G., and Trejo A. 1997. Size and morphology of the Chicxulub impact crater. *Nature* 390:472–476.

Morgan J., Warner M., and Grieve R. A. F. 2002. Geophysical constraints on the size and structure of the Chicxulub impact crater. In *Catastrophic events and mass extinctions: Impacts and beyond*, edited by Koeberl C. and MacLeod K. G. Special Paper #356. Boulder, Colorado: Geological Society of America. pp. 39–46.

Nakashima S., Disnar J. R., Perruchot A., and Trichet J. 1984. Experimental study of mechanism of fixation and reduction of uranium by sedimentary organic matter under diagenetic or hydrothermal conditions. *Geochimica et Cosmochimica Acta* 48: 2321–2329.

Pierazzo E. and Melosh H. J. 1999. Hydrocode modelling of Chicxulub as an oblique impact event. *Earth and Planetary Science Letters* 165:163–176.

Rudnick R. L. and Gao S. 2003. Composition of the continental crust. In *Treatise on geochemistry*, vol. 3, edited by Rudnick R. Amsterdam: Elsevier. pp. 1–64.

Ryder G., Fastovsky D., and Gartner S., editors. 1996. *The Cretaceous-Tertiary event and other catastrophes in Earth history*. GSA Special Paper #307. Boulder, Colorado: Geological Society of America. 569 p.

Schmitt R. T., Wittman A., and Stöffler D. 2004. Geochemistry of drill core samples from Yaxcopoil-1, Chicxulub impact crater, Mexico. *Meteoritics & Planetary Science* 39:979–1001.

Schuraytz B. C., Sharpton V. L., and Marin L. E. 1994. Petrology of impact-melt rocks at the Chicxulub multiring basin, Yucatán, Mexico. *Geology* 22:868–872.

Sharpton V. L., Dalrymple G. B., Marin L. E., Ryder G., Schuraytz B. G., and Urrutia-Fucugauchi J. 1992. New links between the Chicxulub impact structure and the Cretaceous/Tertiary boundary. *Nature* 359:819–821.

Sigurdsson H., Hondt D., and Carey S. 1992. The impact of the Cretaceous/Tertiary bolide on evaporite terrane and generation of major sulfuric acid aerosol. *Earth and Planetary Science Letters* 109:543–559.

Staudigel H. and Hart S. R. 1983. Alteration of basaltic glass: Mechanisms and significance for the oceanic crust-seawater budget. *Geochimica et Cosmochimica Acta* 47:337–350.

Stinnesbeck W., Keller G., Adatte T., Harting M., Stüben D., Istrate G., and Kramar U. 2004. Yaxcopoil-1 and the Chicxulub impact. *International Journal of Earth Sciences* 93:1042–1065.

Stöffler D., Artemieva N. A., Ivanov B. A., Hecht L., Kenkmann T., Schmitt R. T., Tagle R. A., and Wittmann A. 2004. Origin and emplacement of the impact formations at Chicxulub, Mexico, as revealed by the ICDP deep drilling Yaxcopoil-1 and by numerical modeling. *Meteoritics & Planetary Science* 39:1035–1067.

Swisher C. C. III, Nishimura G., Montanari A., Margolis S. V., Claeys P., Alvarez W., Renne P., Cedillo-Pardo E., Maurrasse F. J.-M. R., Curtis G. H., Smit J., and McWilliams M. O. 1992. Coeval $^{40}Ar/^{39}Ar$ ages of 65.0 million years ago from Chicxulub crater melt rock and Cretaceous-Tertiary boundary tektites. *Science* 257:954–958.

Taylor S. R. and McLennan S. M. 1985. *The continental crust: Its composition and evolution*. Oxford: Blackwell Scientific. 312 p.

Tissot B. P. and Welte D. H. 1978. Petroleum formation and occurrence. Berlin: Springer-Verlag. 538 p.

Tuchscherer M. G., Reimold W. U., Koeberl C., Gibson R. L., and de Bruin D. 2004a. First petrographic results on impactites from the Yaxcopoil-1 borehole, Chicxulub structure, Mexico. *Meteoritics & Planetary Science* 39:899–930.

Tuchscherer M. G., Reimold W. U., Koeberl C., and Gibson R. L. 2004b. Major and trace element characteristics of impactites from the Yaxcopoil-1 borehole, Chicxulub structure, Mexico. *Meteoritics & Planetary Science* 39:955–978.

Utzmann A., Hansteen T. H., and Schmincke H.-U. 2002. Trace element mobility during sub-seafloor alteration of basaltic glass from Ocean Drilling Program site 953 (off Gran Canaria). *International Journal of Earth Sciences* 91:661–679.

Ward W. C., Keller G., Stinnesbeck W., and Adatte T. 1995. Yucatán subsurface stratigraphy: Implications and constraints for the Chicxulub impact. *Geology* 23:873–876.

Warren J. 2000. Dolomite: Occurrence, evolution and economically important associations. *Earth-Science Reviews* 52:1–81.

Wilkin R. T., Barnes H. L., and Brantley S. L. 1996. The size distribution of framboidal pyrite in modern sediments: An indicator of redox conditions. *Geochimica et Cosmochimica Acta* 60:3897–3912.

Wittmann A., Kenkmann T., Schmitt R. T., Hecht L., and Stöffler D. 2004. Impact-related dike breccia lithologies in the ICDP drill core Yaxcopoil-1, Chicxulub impact structure, Mexico. *Meteoritics & Planetary Science* 39:931–954.

Wohlgemuth L., Bintakies E., Kück J., Conze R., and Harms U. 2004. Integrated deep drilling, coring, downhole logging, and data management in the Chicxulub Scientific Drilling Project (CSDP), Mexico. *Meteoritics & Planetary Science* 39:791–797.

Zürcher L. and Kring D. A. 2004. Hydrothermal alteration in the core of the Yaxcopoil-1 borehole, Chicxulub impact structure, Mexico. *Meteoritics & Planetary Science* 39: 1199–1221.